THE DE HAAS VAN-ALPHEN EFFECT IN MERCURY

THE DE HAAS-VAN ALPHEN EFFECT IN MERCURY

By

JOHN SEABORN MOSS, B. Sc.

A Thesis

Submitted to the Faculty of Graduate Studies

in Partial Fulfilment of the Requirements

for the Degree

Doctor of Philosophy

McMaster University

May 1968

DOCTOR OF PHILOSOPHY (1968) McMASTER UNIVERSITY
(Physics) Hamilton, Ontario.

TITLE: The de Haas-van Alphen Effect in Mercury

AUTHOR: John Seaborn Moss, B.Sc. (University of Western Ontario)

SUPERVISOR: Dr. W. R. Datars

NUMBER OF PAGES: ix, 103

SCOPE AND CONTENTS:

A study of the Fermi surface of mercury was made using the de Haas-van Alphen effect. The extremal areas of cross-section of the Fermi surface, as determined by field modulation techniques, were in agreement with the relativistic-augmented-plane-wave model of Keeton and Loucks.

The torque de Haas-van Alphen effect was used to search for effects on the de Haas-van Alphen amplitude due to phonons. None were found within experimental error.

The induced torque effect, developed in this study, complements transverse magnetoresistance. The torque signals obtained were dependent on the number of open orbit carriers. The method was used to study the open orbits in mercury.

ABSTRACT

Field modulation techniques were used to observe the de Haas-van Alphen effect in magnetic fields up to 5.5 tesla and at temperatures below 1.1^{o}K. A data acquisition system recorded on magnetic tape the large amount of data necessary for computer fourier analysis of the oscillations. All of the orbits predicted by Keeton and Loucks' model of the Fermi surface of mercury were at least tentatively identified. The data on the β, τ and α orbits were in essential agreement with previous work. The γ and X-face orbits were also investigated in some detail, while tentative identification was made of the μ and T-face orbits. When the data permitted, the areas were fitted to ellipsoids or hyperboloids of revolution by a least squares calculation.

A search was made for modifications to the de Haas-van Alphen theory due to phonons. Accurate torque de Haas-van Alphen amplitude measurements were taken as a function of temperature and magnetic field. The analysis of the results revealed no systematic dependence of either the cyclotron effective mass or the Dingle temperature on temperature from 1.25^{o}K to 4.2^{o}K or on magnetic field from 1.5 tesla to 2.3 tesla. Thus no effects due to phonons were observed.

A method of observing the open orbits in metallic

single crystals was developed and used to observe the open orbits in mercury. The method utilized the eddy currents induced in the sample by the rotation of a magnetic field. This provided a signal which was dependent on the conductivity in the plane perpendicular to the open orbit. The torque amplitude,which indicated the number of open orbit carriers, was used to detect the angular range of the bands of open orbits in mercury. The method was experimentally simple since no special sample geometry was necessary and no electrical connections to the sample were needed.

ACKNOWLEDGEMENTS

I am most grateful to my supervisor, Professor W. R. Datars, for his guidance, help and patience throughout the course of this research.

The support and help of my wife, Mrs. Shirley A. Moss, who has been a partner in this research,is keenly appreciated.

Thanks are due to several faculty members and to the various members of the Fermi surface group here at McMaster for many fruitful discussions. Mr. William Scott has produced many litres of liquid helium and Mr. Clarence Verge constructed most of the circuitry which was used in this work.

The project was supported by a research grant from the National Research Council of Canada. I wish to thank the National Research Council of Canada, the Government of the Province of Ontario and McMaster University for personal financial support.

TABLE OF CONTENTS

LIST OF FIGURES

LIST OF FIGURES (continued)

LIST OF TABLES

CHAPTER I

INTRODUCTION

A. BACKGROUND

The conduction electrons in a metal may be considered as charged fermions in a potential well which has the periodicity and symmetry of the crystal lattice. This potential well is filled to a certain energy, the Fermi energy E_F. The corresponding surface between filled and empty states in momentum space is called the Fermi surface. It is this surface in the case of mercury and the methods used to measure its geometry which are the subject of this thesis. Two techniques were used: the de Haas-van Alphen (dHvA) effect which has also been used in studies of many other materials, and an induced torque method. The induced torque method was developed in this investigation to complement information obtained by other galvanomagnetic effects. Both methods required the use of magnetic fields above ten kilo-oersteds, temperatures below $4.2^{\circ}K$ and high crystal perfection.

It was recognized in the 1930's that both the galvanomagnetic effects and the dHvA effect gave information about the dynamics of conduction electrons. However until the

early 1950's the theory was lacking to make use of these techniques for real metals. The experimental study of the galvanomagnetic effects preceeded the suggestions by Bethe[1] and Peierls[2] that these effects contained Fermi surface information. After 1945, Kohler[3] and Chambers[4] were able to show that specific information could be obtained, and Lifshitz et al[5],[6] [7],[8] laid the theoretical foundations of the method. This work often allowed the connectivity of the Fermi surface to be derived from experimental determinations of the direction and extent of the open orbits. A useful review of high field galvanomagnetic properties has been given by Fawcett[9].

The dHvA effect was discovered by de Haas and van Alphen[10] in 1930 when they observed oscillations of the magnetization of bismuth as a function of magnetic field. In 1933 Peierls[11] showed that the effect was not specific to bismuth, but should, indeed, appear for free electrons. Blackman[12] in 1939 extended this theory while Landau[13] deduced a form for the oscillations for an ellipsoidal Fermi surface. By 1952 Shoenberg[14,15] had used the torque method to measure the oscillations for a number of different metals. In the same year the relation between the area of extremal cross section of the Fermi surface and the dHvA period had been seen by Onsager[16]. A theoretical derivation for a general surface was accomplished by Lifshitz and Kosevich[17] in 1955. In the meantime, Dingle[18] had

derived the expression for the effect of collisions for the case of a scattering time τ.

To a large extent, the success of electronic methods of measuring oscillatory magnetization has depended on the removal of large background signals. In order to do this, two coils are wound in opposition, one containing the sample, the other empty. Using this system and high field pulsed magnets Schoenberg[19] was successful in obtaining oscillations for some of the metals of lower conductivity. Field modulation technique (F.M.T.) in steady field solenoids have been applied to many samples for a wide range of modulation frequencies. Schoenberg[20] has worked above one megahertz while Windmiller and Priestley[21] have used kilohertz modulation. Goldstein, Williamson and Foner[22], Plummer and Gordon[23] and many others have modulated at audio frequencies.

Several methods have been used to study the Fermi surface of mercury. The anomalous skin effect has been reported by Pippard[24]. Approximate areas of some of the pieces of the Fermi surface have been determined using the dHvA effect by Verkin, Laserev and Rudenko[25] on unoriented samples, while Schoenberg[14] has used the magnetic anistropy of the sample to estimate the orientation of a sample. Gustafson, Mackintosh and Zaffarano[26] have shown that the Fermi surface is basically spherical by means of positron annihilation. On the other hand, Ziman[27], from resistivity measurements, concluded that the Fermi surface area was somewhat less than one half the area

for the free-electron model.

While the present investigation was in progress detailed experiments employing magneto-resistance, cyclotron resonance and the dHvA effect were reported. Datars and Dixon[28] and Dishman and Rayne[29] used transverse magneto-resistance to determine the directions and extents of the open orbits. The connectivity and information on some dimensions of the Fermi surface were obtained. Dixon and Datars[30] have identified cyclotron resonance masses with several extremal sections of the Fermi surface. Both torque and F.M.T. were used by Brandt and Rayne[31] to identify three sections of the Fermi surface and to study the long periods in detail. Keeton and Loucks[32] have calculated an approximate Fermi surface shape using the relativistic augmented plane wave method.

B. MERCURY

Mercury has the distinction of having the lowest melting point ($-39^{\circ}C$) of the metallic elements and a low Debye temperature ($60-90^{\circ}K$). The crystal structure is rhombohedral and no phase transformations occur on cooling to below $4.2^{\circ}K$ at room pressure. A tetragonal phase has been shown to occur if the pressure is raised to 10,000 atmospheres at $4.2^{\circ}K$[33]. This transformation is probably martensitic and does not occur for the pressures used in Fermi surface experiments. The lattice parameters of mercury have been measured at $5^{\circ}K$ and atmospheric pressure by Barrett[34], who

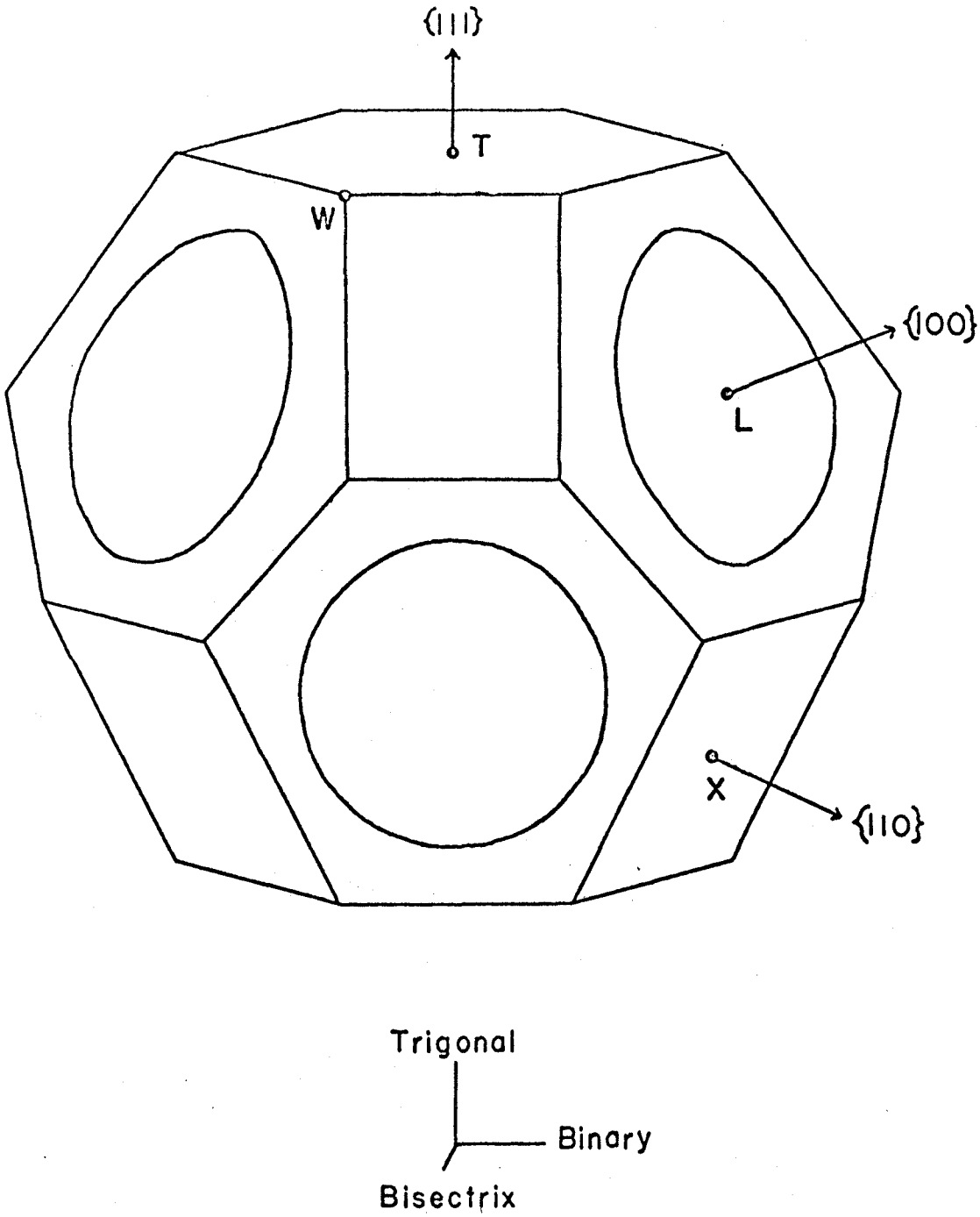

FIGURE 1

THE FIRST BRILLOUIN ZONE OF MERCURY
SHOWING THE INTERSECTIONS WITH THE
FREE ELECTRON SPHERE

quotes

$$a = 2.9963\ A^{o}$$

$$\alpha = 70^{o}\ 44.6'$$

where a is the lattice constant and α is the rhombohedral angle.

The Brillouin zone, shown in Figure 1, has the same symmetry as the crystal lattice and is given by Jones[35]. The following convention is used to define directions in real and reciprocal space. A direction in real space is designated by [l m n] and a plane in real space by (l m n), with no commas. In reciprocal space directions are (l, m, n), in this case with commas.

Using the free electron model, the spherical Fermi surface cuts the pseudo-hexagonal L-faces, leaving six electron lenses in the second zone and a multiply connected first zone hole surface as shown in Figure 1. The T- and X-faces do not make contact with the sphere, but the separation is very small.

The band structure calculation of Keeton and Loucks predicts contact of the Fermi surface with both the T- and X-faces as shown in Figure 2. Also, this calculation indicates that the connecting arms of the first zone are bent in toward the centre of the X-faces as shown in Figure 2. The closed orbits that are supported by this model were given by Dixon[36] and are shown in Figure 3. The β hole orbit, which circles the arms situated along the X-face sides have

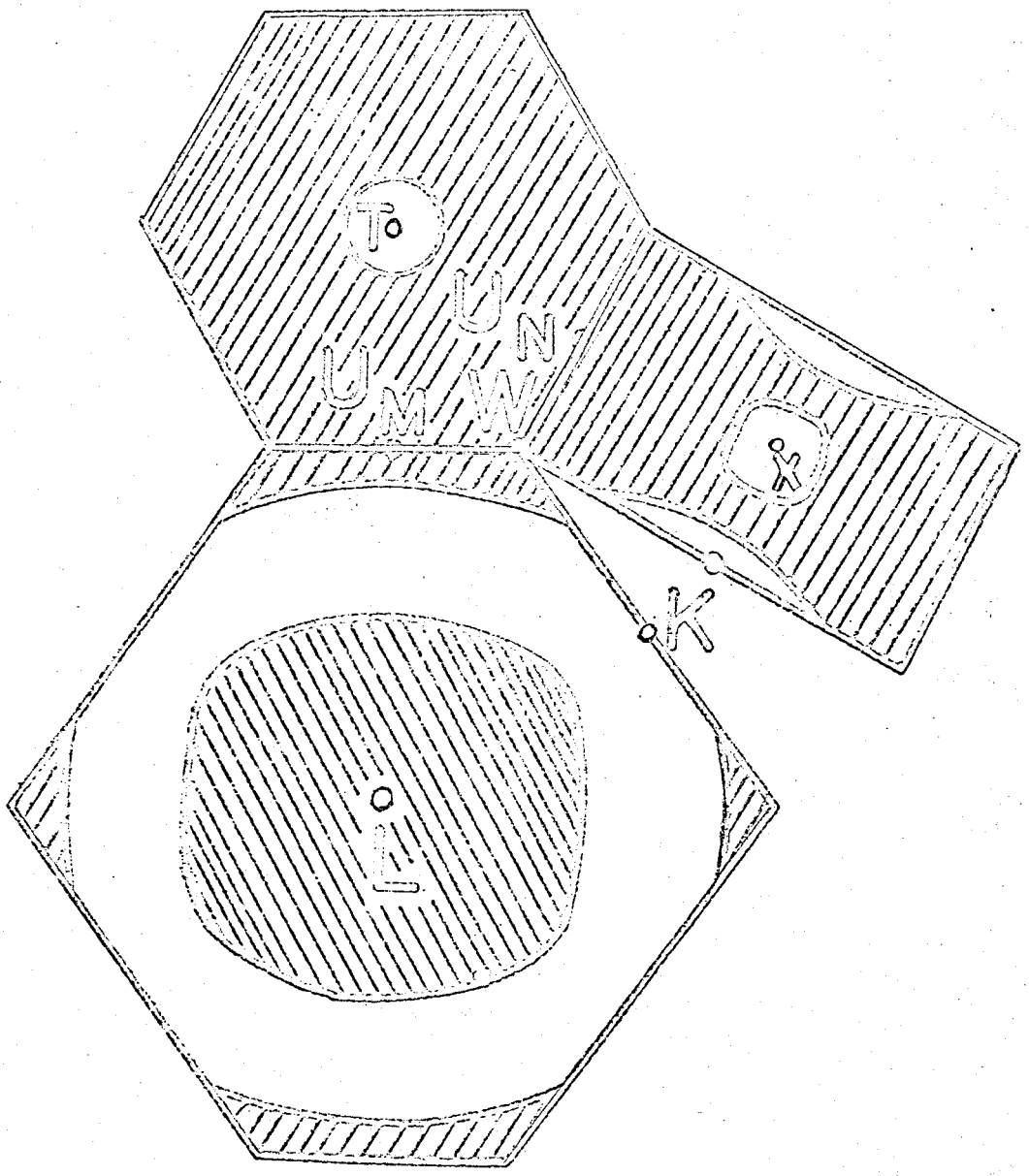

Figure 2

Brillouin Zone Faces Showing the Intersections Between the Zone Faces and the Fermi Surface as Predicted by Keeton and Loucks

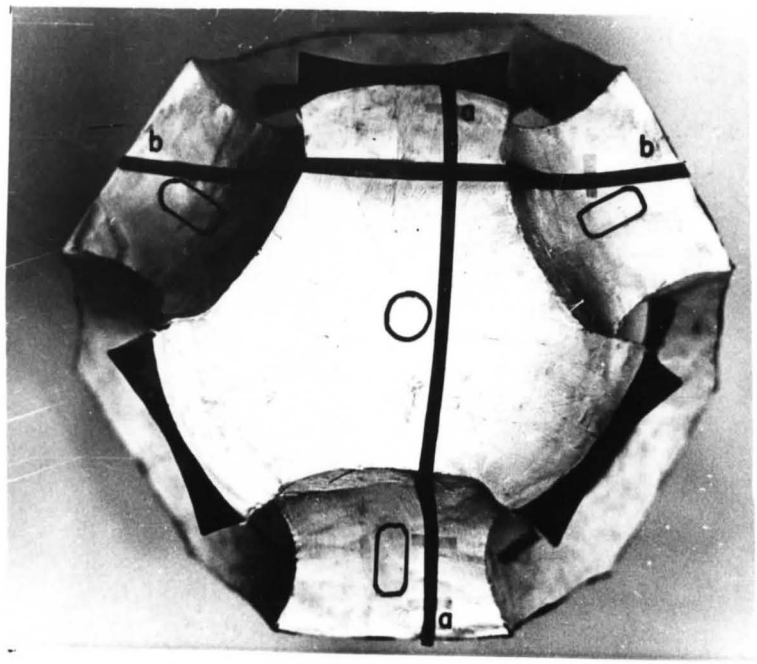

(a) Showing open orbits

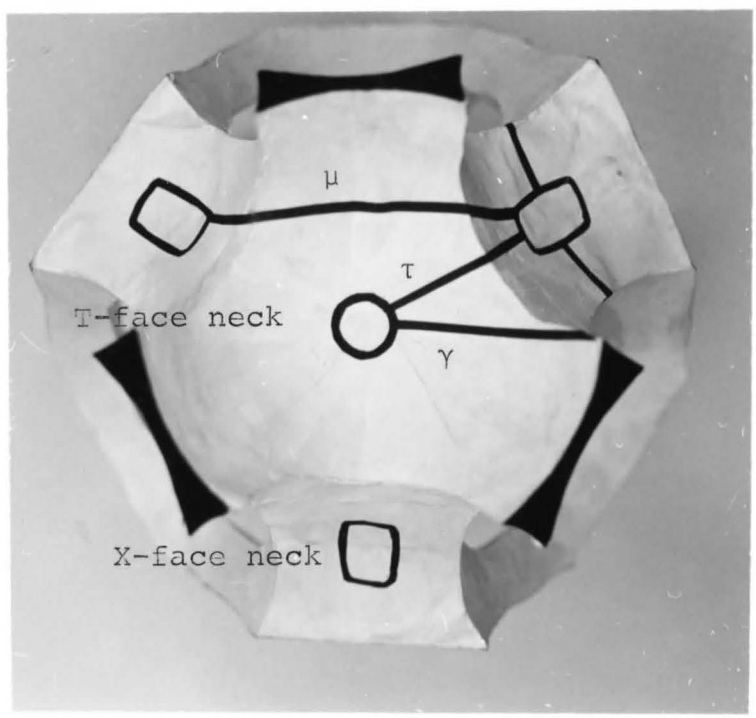

(b) Showing closed orbits

Figure 3

The First Zone Hole Surface of Mercury (Nearly Free Electron Approximation) (after Dixon)

been seen by Brandt and Rayne using the dHvA effect and Poulsen and Dixon,[37] using quantum oscillations. The dHvA oscillations were fitted using a pseudo-potential calculation. Poulsen has used a least square fit to an hyperboloid of revolution, obtaining a very close fit to the data. This latter procedure was designed to give parameters for use with information on other parts of the Fermi surface and did not give direct parameters of the crystal potential.

The α orbits circle the second zone electron lenses. They have been seen by Dixon using cyclotron resonance, and the masses were fitted to a mass ellipsoid of revolution. Brandt and Rayne detected these carriers in F.M.T. data but no fitting was attempted.

Brandt and Rayne detected the τ orbits over a wide range of angle in several planes. Again no fits were made. The orbits pass through the holes in the L-, T- and X-faces and are boomerang shaped. The minimum area is normal to the binary axis.

A hole orbit is possible which passes through two L-faces and one T-face. This orbit is the γ orbit, and has its minimum near the bisectrix direction. Its angular range in the binary-bisectrix plane is an indication of the spreading of the L-face holes onto the X-faces. The γ orbits have been seen by Dixon using cyclotron resonance.

The μ orbit is a hole orbit with its minimum area approximately normal to the bisectrix direction. This orbit

crosses the T-face, passes through an L-face, then an X-face hole, crosses back across the other side of the same T-face, through an X-face hole and finally an L-face hole. Keeton and Loucks' model predicts a first zone electron orbit around the neck where the first zone surface intersects the zone boundary. A similar hole orbit is supported by the neck at the T-face. An orbit at the L-face, which is extremely sensitive to the amount of overlap of the L-face intersection onto the X-face, probably does not exist. Previous to this investigation the γ, μ, X-face and T-face orbits have not been identified.

Three open orbits have been detected, using transverse magneto-resistance, lying along the (1,0,0),(1,1,0) and $(1,\bar{1},0)$ directions. These directions are given in terms of the primitive reciprocal lattice vectors. A fourth orbit has been suggested along the (1,2,3) direction.

In this investigation the torque dHvA method was used in a search for real phonon effects using accurate amplitude measurements as a function of amplitude and magnetic field. The β orbit was used for the amplitude measurements.

The field modulation technique study was aimed at obtaining accurate geometric fits for the τ, γ, X-face and α orbits, and identifying other orbits.

The induced torque technique was developed in this study. This method was used to substantiate the previous work on the open orbits in mercury and to delimit accurately the angular extent of some of these bands of open orbits.

CHAPTER II

THEORY

A. ELECTRONS IN A MAGNETIC FIELD

In the introduction it was stated that the conduction electrons in a metal are charged fermions in a potential well. These electrons interact with the ions, the bound electrons, and each other. The major effects of the bound electrons are to neutralize some of the ionic charge and to screen the cores such that the potential is almost constant over most of the unit cell. The eigenstates of such a system are Bloch functions:

$$\psi_{\bar{k}} = e^{i\bar{k}\cdot\bar{r}}\, Y_{\bar{k}}(\bar{r}) \qquad \text{II.1}$$

When the effects of interactions with the other conduction electrons are taken into account it is found (Pines[38]) that the lifetime of the pseudo-particles varies inversely as $(k-k_F)^2$ where k_F is the wave number of the particle state at the Fermi surface. Thus the states near the Fermi surface, that is, the states that define the Fermi surface, still have a small energy spread. Impurity scattering, on the other hand, does affect the states at the Fermi surface and this effect has been accounted for under a variety of approximations (Dingle[18], Williamson[39]). The effect of scattering by phonons is thoroughly masked

by the effect of the thermal smearing of the occupation of the states about the Fermi surface. Even at room temperature most features of the Fermi surface are large compared with thermal smearing. It is the methods of measurement which require very low temperatures and extremely high crystal perfection. At somewhat higher temperatures small details of the Fermi surface may be of the order of the smearing.

The effect of a magnetic field on the conduction electrons causes a rearrangement of the electron states in momentum space. The effect on a given state of wave vector $\bar{k}$ is given by:

$$\dot{\bar{k}} = \frac{e}{\hbar} \bar{V} \times \bar{B} \qquad \text{II-2}$$

Where: e is the electronic charge

$\bar{V} = \nabla_{\bar{k}} \mathcal{E}$ = the velocity of the electron in real space.

Thus the k vector of the state is confined to the intersection of a plane normal to the magnetic field and the isoenergetic surface corresponding to the particular k vector.

The cyclotron frequency ω_c is defined by

$$\frac{2\pi}{\omega_c} = \frac{\hbar}{eB} \int_{\text{orbit}} \frac{dk}{v_\perp} \qquad \text{II.3}$$

where

$$v_\perp = \frac{1}{\hbar} \frac{d\mathcal{E}}{dk_\perp} \qquad \text{II.4}$$

is the component of $\bar{v}$ which is perpendicular to $\bar{H}$ and to the Fermi surface tangent at k. For free electrons

$$\omega_c = \frac{eB}{m} \quad . \qquad \text{II.5}$$

This expression is used to define a cyclotron mass

$$m^* = \frac{eB}{\omega_c} \qquad \text{II.6}$$

for electrons affected by a potential. It is a property of the orbit, and, in terms of the area, A, in k-space of the orbit, and its energy, $\mathcal{E}$ it is

$$m^* = \frac{\hbar^2}{2\pi} \frac{\partial A}{\partial \mathcal{E}} \qquad \text{II.7}$$

Equation II.2 states that the representative point in k-space traverses an orbit in a plane perpendicular to $\bar{B}$. Integrating II.2 with respect to time gives

$$\bar{k} = \frac{e}{\hbar} \bar{r} \times \bar{B}, \qquad \text{II.8}$$

which is the relation between the k-space orbit and the projection of the real space orbit on a plane perpendicular to $\bar{B}$.

There are several types of orbit topography in k-space. Closed orbits are quantized orbits and are contained within the volume of the Brillouin zone. In a multiply-connected Fermi surface there may be open orbits which extend for an infinite distance through momentum space. Also there may be orbits which are closed but extend through the extended zone scheme for some distance.

The high-field region may be defined more accurately

by comparing the scattering time τ with characteristic times of the orbit. For the case of closed orbits the definition is

$$\gamma = \frac{1}{\omega_c \tau} \ll 1 \ . \qquad \text{II.9}$$

This states, semi-classically, that the electron has accomplished at least one radian of the orbit in the time τ. For open orbits the expression is

$$\gamma = \frac{1}{\tau \omega_o} \ll 1 \qquad \text{II.10}$$

where $\omega_o = \frac{2\pi}{T_o}$ and T_o is the time between Bragg reflections. In both cases it is necessary to use sufficiently high magnetic fields to satisfy the inequality by a factor of 5 or 10 in order to obtain clear results.

B. MAGNETORESISTANCE

When an electric field is also applied to the sample the current in the sample is determined by the conductivity tensor in the expression

$$J_i = \sigma_{ij} E_j \ . \qquad \text{II.11}$$

The Onsager relation in the presence of a magnetic field states that

$$\sigma_{ij}(B) = \sigma_{ji}(-B) . \qquad \text{II.12}$$

Each element of the σ_{ij} tensor may be expanded in terms of γ.

$$\sigma_{ij} = a_{ij}^{o} + a_{ij}^{1} \gamma + a_{ij}^{2} \gamma^2 + \ldots \quad . \qquad \text{II.13}$$

Only the dependence on B of each of the σ_{ij} is necessary for

our purposes. Two situations will be considered, the case where the direction of $\bar{B}$ defines no open orbits and the case where there are open orbits.

Consider the field $\bar{B}$ to be in the z-direction. In the absence of open orbits the a^{o}_{ij} coefficients are zero in the limit of $\gamma \to 0$ except for σ_{zz}. The application of an electric field causes a displacement of the Fermi surface. The effect of the magnetic field is to cause this displacement to rotate about the direction $\bar{B}$ as given by II.2. Thus, if $\omega_c \tau >> 1$ there will be no net current in the x-y plane. That is

$$a_{xj} = a_{yj} = 0. \qquad \text{II.14}$$

As

$$\sigma_{ii}(B) = \sigma_{ii}(-B)$$

there can be no linear terms in a_{ii}. Combining this with II.2 and II.14 gives

$$\lim_{\gamma \to 0} \sigma_{ij} = \begin{pmatrix} a^{2}_{xx}\gamma^2 & a^{1}_{xy}\gamma & a^{1}_{xz}\gamma \\ -a^{1}_{xy}\gamma & a^{2}_{yy}\gamma^2 & a^{1}_{yz}\gamma \\ -a^{1}_{xz}\gamma & -a^{1}_{yz}\gamma & a^{o}_{zz} \end{pmatrix} \qquad \text{II.15}$$

where only the leading terms have been retained. The resistivity tensor is obtained by inverting σ_{ij}. The field dependencies of the matrix elements, keeping only the high order terms, are

$$\lim_{B \to \infty} \rho_{ij} = \begin{pmatrix} \sim B^{o} & \sim B^{1} & \sim B^{o} \\ \sim B^{1} & \sim B^{o} & \sim B^{o} \\ \sim B^{o} & \sim B^{o} & \sim B^{o} \end{pmatrix} \qquad \text{II.16}$$

By carrying out the integration for a^1_{xy} it is found that

$$a^1_{xy}\gamma = \frac{ec}{B\Omega}\,(n_e - n_h).$$

Ω is the volume of the unit cell and n_e and n_h are the number of electrons and holes, respectively, per unit cell. For a compensated metal the terms a^1_{xy} are therefore zero, giving

$$\lim_{\gamma\to 0} \sigma_{ij} = \begin{pmatrix} a^2_{xx}\gamma^2 & a^2_{xy}\gamma^2 & a^1_{xz}\gamma \\ -a^2_{xy}\gamma^2 & a^2_{yy}\gamma^2 & a^1_{yz}\gamma \\ -a_{xz}\gamma & -a^1_{yz}\gamma & a^o_{zz} \end{pmatrix} \qquad \text{II.17}$$

The corresponding resistivity tensor has the following dependence on B

$$\lim_{B\to\infty} \rho_{ij} = \begin{vmatrix} \sim B^2 & \sim B^2 & \sim B \\ \sim B^2 & \sim B^2 & \sim B \\ \sim B & \sim B & \sim B^o \end{vmatrix} \qquad \text{II.18}$$

Next, let us assume that there is an open orbit extending in k-space along the x-direction. Since the motion of the representative point in k-space is constrained to the x-axis, II.8 shows that the open orbit cannot carry current in the x-direction. The terms containing n_e-n_h will no longer be zero for a compensated metal, as the nature of a carrier on an open orbit is undefined. The open orbit can carry current in the y-direction and terms containing a^o_{yj} are no longer zero. Thus, for both compensated and uncompensated metals

$$\lim_{\gamma\to 0} \sigma_{ij} = \begin{pmatrix} a^{2}_{xx}\gamma^{2} & a^{1}_{xy}\gamma & a^{1}_{xz}\gamma \\ -a^{1}_{xy}\gamma & b^{o}_{yy} & b^{o}_{yz} \\ -a^{1}_{xz}\gamma & b^{o}_{yz} & b^{o}_{zz} \end{pmatrix} \qquad \text{II.19}$$

when there is an open orbit in the x-direction. The resistivity tensor in this case goes as

$$\lim_{B\to\infty} \rho_{ij} = \begin{pmatrix} \sim B^{2} & \sim B & \sim B \\ \sim B & \sim B^{o} & \sim B^{o} \\ \sim B & \sim B^{o} & \sim B^{o} \end{pmatrix} \qquad \text{II.20}$$

C. dHvA THEORY

The Bohr-Somerfeld quantization relation,

$$\oint \bar{p}\cdot d\bar{r} = (n+\gamma)2\pi\hbar, \qquad \text{II.21}$$

may be used to find the distribution in k-space of closed orbits of high wave number.

The conjugate momentum is

$$\bar{p} = \hbar\bar{k} + e\bar{A} \qquad \text{II.22}$$

and γ is a phase factor. The choice of the gauge

$$\bar{A} = (0, Bx, 0) \qquad \text{II.23}$$

gives

$$\bar{B} = \nabla \times \bar{A}$$

$$= (0, 0, B)$$

The area of the allowed orbit in k-space is

$$A(n) = \frac{2\pi eB}{\hbar}\ (n+\gamma). \qquad \text{II.24}$$

The electron states are thus condensed onto allowed orbits in the x-y plane while the component of $\bar{k}$ along the

magnetic field, k_z, is unchanged. Thus the allowed orbits lie along tubes.

Combining II.6 and II.7 results in an expression for $\delta\mathcal{E}$ in terms of δA

$$\delta\mathcal{E} = \frac{\hbar^2\omega_c}{2\pi eB}\,\delta A \quad . \qquad \text{II.25}$$

This is integrated and the term derived from k_z added to give

$$\begin{aligned}\mathcal{E} &= \frac{\hbar^2\omega_c}{2\pi eB}\,A(n) + f(k_z) \\ &= \hbar\omega_c\,(n+\gamma) + f(k_z)\end{aligned} \qquad \text{II.26}$$

Any deviation from ω_c = constant for very small n may be absorbed into γ.

As the magnetic field is changed the energy of the electron state changes in proportion to the change in $|\bar{B}|$. If the energy of a given state is raised above E_F, the Fermi energy, then that state will empty. Since the tube of allowed states and the Fermi surface are both equipotentials all the states on that orbit will empty at the same time. If these were the only states of the system the Fermi level would be forced up rather than allow the states to empty. E_F is, however, determined by the Fermi surface as a whole. Because of this the reduction of the oscillation amplitude by variations in E_F is negligible.

Thus the slices along k_z of the Fermi surface each give rise to a series of periodic changes in the free energy. These changes only add in phase for the maximum or minimal

areas of the Fermi surface. These changes are periodic in 1/B as is seen from II.24.

Lifshitz and Kosevich[17] have evaluated the free energy for a system of electrons in perfectly sharp Landau levels, but at finite temperatures. This is a reasonable model as phonon broadening is small compared with the thermal smearing of the Fermi-Dirac occupation function.

The free energy per unit volume of the system is given by

$$F = NE_F - KT \sum_i \ln\left(1 + e^{(E_F - \mathcal{E}_i)/KT}\right) \qquad \text{II.27}$$

where E_F is the Fermi energy

N is the number of electrons in the system.

The energy of the state i depends on the quantum number of the appropriate Landau level and a function of the component of k along the magnetic field. Thus:

$$\mathcal{E}_i = \mathcal{E}(n+\gamma, k_z) \; . \qquad \text{II.28}$$

Converting the sum over momentum space to a sum over Landau levels and an integral over k_z gives

$$F = NE_F - KT \int_{-\infty}^{+\infty} \left\{\frac{eB}{2\pi^2\hbar} \sum_{n=0}^{\infty} \ln\left(1 + \exp\left[\{E_F - \mathcal{E}(n+\gamma, k_z)\}/KT\right]\right)\right\} dk_z . \qquad \text{II.29}$$

This integrand may be evaluated for each of its fourier components separately. Using the Poisson summation formula to accomplish this gives:

$$F = NE_F - KT \int_{-\infty}^{+\infty} \left\{\frac{eB}{2\pi^2\hbar} \int_0^{\infty} \ln\left(1+\exp\left[\{E_F - \mathcal{E}(x+\gamma, k_z)\}/KT\right]\right) dx\right\} dk_z$$

$$-2KT \sum_{s=1}^{\infty} \int_{-\infty}^{+\infty} \{\frac{eB(-1)^s}{2\pi^2\hbar} \int_{-\infty}^{+\infty} \ln(1+\exp[\{E_F - (x+\gamma, k_z)\}/KT])\cos 2\pi x s dx\} dk_z \quad \text{II.3}$$

where s runs over the Fourier components. The third term is the integral which gives rise to the oscillatory part of the free energy. Using the Fermi-Dirac distribution function,

$$f^o(\ ) = \frac{1}{e^{(\ -E_F)/KT}} \quad \text{II.31}$$

$$= \frac{KT\partial \ln(1+e^{(E_F-\ )/KT})}{\partial} ,$$

and intdgrating twice by parts results in the oscillatory part of the free energy:

$$F_{osc} = -2KT \sum_{s=1}^{\infty} \int_{-\infty}^{+\infty} \{\frac{eB(-1)^s}{2\pi^2\hbar} \int_{0}^{\infty} \frac{\cos 2\pi x s}{4\pi^2 s^2 KT} [f^o(\ ) \frac{\partial^2}{\partial x^2} + \frac{\partial f^o}{\partial x} \frac{\partial}{\partial x}] dx\} dk_z \quad \text{II.32}$$

The energy of a given state is:

$$(x+\gamma, k_z) = (x+\gamma)\hbar\omega_c + f(k_z).$$

$$\frac{\partial}{\partial x} = \hbar\omega_c$$

$$\frac{\partial^2}{\partial x^2} = 0$$

Lowering the lower limit of inner integration to $-\infty$ yields

$$F_{osc} = -2KT \sum_{s=1}^{\infty} \int_{-\infty}^{+\infty} \{\frac{eB(-1)^s \omega_c}{8\pi^4 s^2 KT} \int_{-\infty}^{\infty} \cos\ 2\pi x s \frac{\partial f^o}{\partial x} dx\} dk_z \quad \text{II.33}$$

The inner integral may now be expanded, simplified and integrated to give:

$$F_{osc} = 2KT \sum_{s=1}^{\infty} \int_{-\infty}^{+\infty} \frac{eB(-1)^s \cos\left(\frac{s\hbar A(E_F, k_z)}{eB}\right)}{4\pi^2 s\hbar \sinh\left(\frac{2\pi^2 sKT}{\hbar\omega_c}\right)} dk_z , \qquad \text{II.34}$$

where $A(E_F,k_2)$ is the part of the area of the plane perpendicular to $\bar{B}$ at k_z that is bordered by the intersection of this plane and the Fermi surface.

This is a Fresnel integral and it may be evaluated for each region along k_z corresponding to a maximum or a minimum of the area $A(E_F,k_z)$. If one assumes that ω_c does not vary rapidly with k_z in a region about k_o, the value of k_z corresponding to the extremal area A, then

$$F_{osc} = 2KT \sum_{s=1}^{\infty} (-1)^s \left(\frac{eH}{2\pi s\hbar}\right)^{3/2} \frac{1}{\sinh\left(\frac{2\pi^2 sKT}{\hbar\omega_c}\right)} \qquad \text{II.35}$$

$$\times \left|\frac{\partial^2 A}{\partial k_z^2}\right|_{k_z=k_o}^{-\frac{1}{2}} \cos\left(\frac{s\hbar}{eH} A_o \mp \pi/4\right)$$

The above expression considers perfectly sharp Landau levels. In the case of an isotropic, energy and momentum independent scattering time τ each term in the expression in II.35 must be multiplied by $\exp(-\frac{S}{\omega_c \tau})$ (Williamson[39]).

Effects due to the spin of the electrons split the Landau levels into two levels, equally spaced above and below the unsplit level. An additional factor is

$$\cos\left(\frac{\Pi s g m_c}{2m_e}\right) \qquad \text{II.36}$$

where g is the g-factor for the conduction electrons.

m^* is the effective mass

m_e is the electron mass.

The complete expression for the oscillatory free energy is

$$F_{osc} = 2KT \sum_{s=1}^{\infty} (-1)^s \left(\frac{eB}{2\pi s\hbar}\right)^{3/2} \left|\frac{\partial^2 A(E_F,k_z)}{\partial k_z^2}\right|_{A=A_o}^{-\frac{1}{2}} \frac{\cos\left(\frac{s\hbar}{eB} A_o \mp \frac{\pi}{4}\right)}{\sinh\left(\frac{2\pi^2 sKT}{\hbar\omega_c}\right)}$$

$$\times \exp\left(\frac{-s}{\omega_c\tau}\right) \cos\left(\frac{\pi s g m_c}{2m_e}\right) \qquad \text{II.37}$$

D. EXPRESSIONS FOR TORQUE AND MAGNETIZATION

The expression II.37 may be differentiated by H to give the magnetization M , or by θ, an angle in space, to give the torque per unit volume of sample. In either case the argument of the oscillatory term is not changed, though the amplitude factor in the torque case becomes zero along symmetry directions.

The oscillatory part of the torque is given by:

$$L_{osc} = \left(\frac{\partial F_{osc}}{\partial \theta}\right)_H$$

$$= 2KT \sum_{s=1}^{\infty} \left|\frac{\partial^2 A(E_F,k_z)}{\partial k_z^2}\right|_{A=A_o}^{-\frac{1}{2}} \frac{\partial A_o}{\partial \theta} \frac{1}{2\pi} \left(\frac{eB}{2\pi s\hbar}\right)^{\frac{1}{2}} (-1)^{s-1} \qquad \text{II.38}$$

$$\times \frac{\sin\left(\frac{s\hbar A_o}{eB} \mp \pi/4\right) \cos\left(\frac{\pi s g m_c}{2m_e}\right)}{\sinh\left(\frac{2\pi^2 sKT}{\hbar\omega_c}\right) \exp\left(\frac{s}{\omega_c\tau}\right)}$$

The other terms are small.

The magnetization is given by:

$$M_{osc} = -\nabla_B F = -\left(\frac{\partial F}{\partial B}\right)_{T,V} \qquad \text{II.39}$$

provided that magnetic interactions are small.

It is not necessary that the magnetization be along the magnetic field direction. Since the magnetization of each segment of the Fermi surface may be in different directions it is possible to orient the detection coils in a modulation experiment to eliminate a certain dominant period or maximize the signal to noise ratio for a signal of low amplitude.

The magnitude of the magnetization is obtained by differentiating II.37 by B. The result is

$$M = 2KT \sum_{s=1}^{\infty} A_o (-1)^{s-1} \left(\frac{e}{s\hbar}\right)^{\frac{1}{2}} (2\pi)^{-3/2} B^{-\frac{1}{2}} \left| \frac{\partial^2 A(E_F, k_z)}{\partial k_z^2} \right|^{-\frac{1}{2}}_{A=A_o} \times \frac{\sin\left(\frac{s\hbar}{eB} A_o \mp \pi/4\right) \exp\left(\frac{-s}{\omega_c \tau}\right) \cos \frac{\pi s g m_c}{2m_e}}{\sinh\left(\frac{2\pi^2 sKT}{\hbar\omega_c}\right)} \qquad \text{II.40}$$

CHAPTER III

INDUCED TORQUE EFFECT

In the conventional method for determining the transverse magnetoresistance of a metal a known current is passed through the sample and the voltage is measured between two separate contacts along the sample. This voltage is proportional to the diagonal terms ρ_{xx} or ρ_{yy} of II.16 for an uncompensated metal and of II.18 for a compensated metal. The reason for the difference in the ρ_{yy} terms of compensated and uncompensated metals is the difference in the term σ_{xy} which appears in the denominator during the inversion of the conductivity tensor to obtain the resistivity tensor. When the magnetic field direction defines an open orbit along the x axis, the open orbit carriers only conduct in the y-z plane. For both compensated and uncompensated metals the open orbits result in changes in the magnetoresistance which enable one to determine the directions of the open orbits. For a compensated metal the transverse magnetoresistance saturates when the field is perpendicular to an open orbit, and is proportional to B^2 otherwise. The size of the open orbit only causes a minor change in the degree of saturation.

The induced torque effect is a method of observing open orbits in metals which complements transverse magnetoresistance. The sample is suspended on a quartz rod connected to a torsion meter. A magnetic field is applied to the sample

and rotated slowly through the z direction about the vertical axis. Thus $\frac{d\bar{B}}{dt}$ is perpendicular to both $\bar{B}$ and the vertical, or torque axis,as shown in Figure 4. This is related to the electric fields within the sample by Faraday's Law of Induction

$$\nabla \times \bar{E} = - \frac{d\bar{B}}{dt} , \qquad \text{III.1}$$

with the boundary conditions that $J_{\perp} = 0$. The field $\bar{E}$ drives loops of current around the direction of $\frac{d\bar{B}}{dt}$ which is in the x direction. The magnetic moment of this current distribution is

$$\vec{m} = \frac{1}{2} \int \bar{r} \times \bar{J}(\bar{r}) \, d^3r \qquad \text{III.2}$$

which is co-linear with $\frac{d\bar{B}}{dt}$. The torque is

$$\bar{L} = \bar{m} \times \bar{B} \qquad \text{III.3}$$

about the y axis.

For a compensated metal the current loops are normal to $\frac{d\bar{B}}{dt}$. In this case the current distribution and thus the torque, is determined by $\frac{1}{\rho_{yy}}$ and $\frac{1}{\rho_{zz}}$, if $\frac{1}{\rho_{yz}}$ is assumed to be negligible. ρ_{zz} is always small, so the field direction is always a direction of high conductivity. Changes in $\frac{1}{\rho_{yy}}$, which has the same dependence on B as σ_{yy}, are reflected in the torque. Thus, the torque is proportional to γ^{o} when there is an open orbit defined by $\bar{B}$ and to γ^{2} otherwise. Thus the torque signal observed when the field is set perpendicular to an open orbit is dependent on the strength of the open orbit.

When the sample is an uncompensated metal the currents are not confined solely to the y-z plane. In this case there are large Hall terms which produce voltages in the x-direction.

In the case of the conventional magnetoresistance geometry this voltage appears across the sample but for the induced torque geometry the voltage at opposite sides of the sample is oppositely directed. Thus currents may flow in the x-z plane as well as the y-z plane and the currents are determined by several terms of the resistivity tensor. However, currents in the y-z plane still cause a torque about the y direction.

In both compensated and uncompensated metals, there will be a plane of high conductivity perpendicular to the open orbit direction due to the open orbit carriers which does not exist in the absence of an open orbit. There will be no contribution to the torque from currents which are perpendicular to either $\bar{B}$ or the torque axis. Open orbits may be measured by the induced torque in both compensated and uncompensated metals.

To obtain a general solution, the current distribution in the sample is given by Maxwell's equations (Smythe[41]).

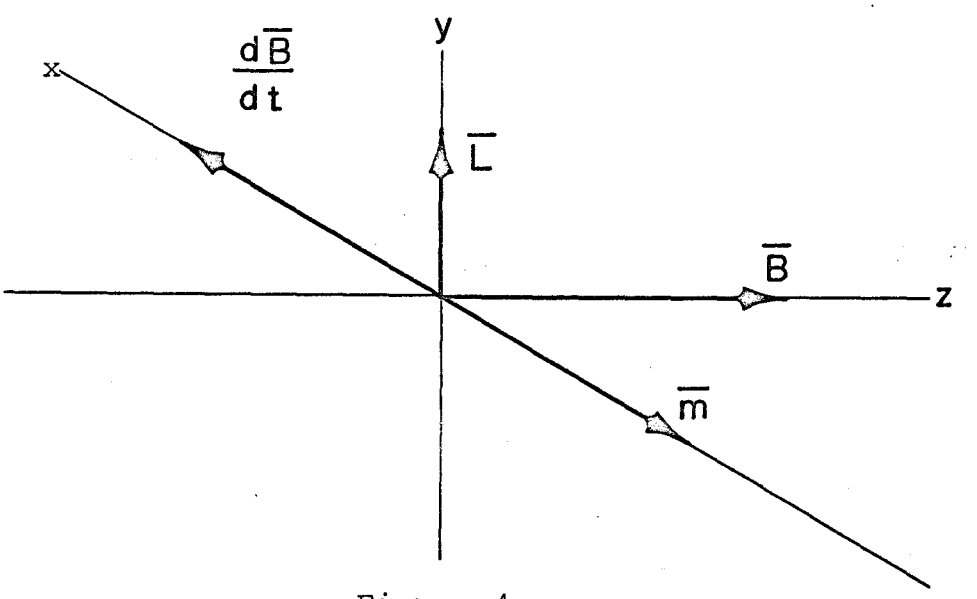

Figure 4
Geometry of the Induced Torque Effect.

The two equations

$$\nabla \times \bar{H} = \bar{J} + \frac{\partial \bar{D}}{\partial t} \qquad \text{III.4}$$

$$\nabla \times \bar{E} = - \frac{\partial \bar{B}}{\partial t} \qquad \text{III.1}$$

where $\frac{\partial \bar{D}}{\partial t}$ is zero for slowly varying fields, must be solved for a tensor $\bar{\bar{\sigma}}$ and the boundary condition that $\bar{J}$ be parallel to the sample surface.

When the conductivity is isotropic III.4 and III.1 combine to give

$$\nabla^2 \bar{B} = \sigma\mu \frac{\partial B}{\partial t} \qquad \text{III.5}$$

where $\bar{J} = \sigma \bar{E}$

and $\bar{B} = \mu \bar{H}$.

III.5 is difficult to solve for general boundary conditions. For the following simple conditions the problem can be solved from Maxwell's equations. If also the sample symmetry is cylindrical about $\frac{d\bar{B}}{dt}$ then III.1 allows evaluation of the current, and, therefore the torque. Integration of both sides of III.1 over a general surface, s, and an application of Stokes' law give

$$- \int_s \frac{d\bar{B}}{dt} \, d\bar{a} = \oint_c \bar{E}.d\bar{l} \qquad \text{III.6}$$

where C is the boundary of the surface s. When the magnet is rotated at angular frequency ω, the left hand side of III.6 becomes

$$\frac{d}{dt}\int_s B \sin\omega t \, da$$

$$= \omega BA$$

where A is the area of the surface s. The right hand side of III.6 is integrated for a circular path concentric with the cylindrical axis of symmetry. The result is

$$J = \frac{\sigma\omega Br}{2}, \qquad \text{III.7}$$

directed perpendicular to $\frac{d\bar{B}}{dt}$ and $\bar{r}$. The torque about the vertical axis is

$$\bar{L} = \frac{1}{2}\left[\int \bar{r} \times \bar{J}(\bar{r}) \, d^3r\right] \times \bar{B}$$

$$= \frac{\pi\sigma\omega B^2 R^4 \ell}{8} \hat{y} \qquad \text{III.8}$$

for a cylinder of length ℓ and radius R. The torque per unit volume is $\frac{\sigma\omega B^2 R^2}{8}$, and its dependence on R emphasizes the extra signal gained by using a large sample.

$$\bar{L} = \frac{2\pi\sigma\omega B^2 R^5}{15} \hat{y} \qquad \text{III.9}$$

for a sphere of radius R.

A. EXPERIMENTAL APPARATUS

The experiments were performed using a 12-inch Pacific Electric Motor Corp. electromagnet with a two-inch pole gap and equipped with a motor drive for rotation from 0.0016 to 0.014 rad/sec maintained at 0.8 to 1.0 webers per meter^2 to avoid dHvA oscillations. Temperatures below 1.5°K were attained by pumping on the liquid helium bath. The torque

magnetometer was of the design of Condon and Marcus[42], modified as described by Vanderkooy[40]. In order to accomplish a solid angle experiment it was necessary to rotate the sample about an horizontal axis.

An apparatus was constructed to rotate the crystal about an horizontal axis without removing the sample from the dewar or subjecting the quartz suspension or jewelled bearings to undue strain. This apparatus is shown in Figure 5(a). The support rods were mounted such that the lateral position of the bottom of the pins shown in Figure 5(b) was adjustable to an accuracy of a few hundredths of an inch. In this way these pins were set so as not to touch the sides of the holes in the sample holder. When the sample holder was raised as in Figure 5(c) the pins made firm contact with the sample holder, preventing any rotation. In this position a blade on the end of a vertical shaft made contact with a slot in a worm gear in the sample holder. Rotation of the shaft caused rotation of the gear and thus of the sample drum. The sample was usually rotated in 2 degree steps with an accuracy of 0.2 degree . The slide shown in Figure 5(d) raised the lower portion of the suspension, disconnecting it from the upper quartz rod and thus from the bearing at the same time as the pins and driver blade were engaged. Both the rod which moved the slide and the rod which rotated the blade were passed through simple O-ring seals at the top plate.

(a)

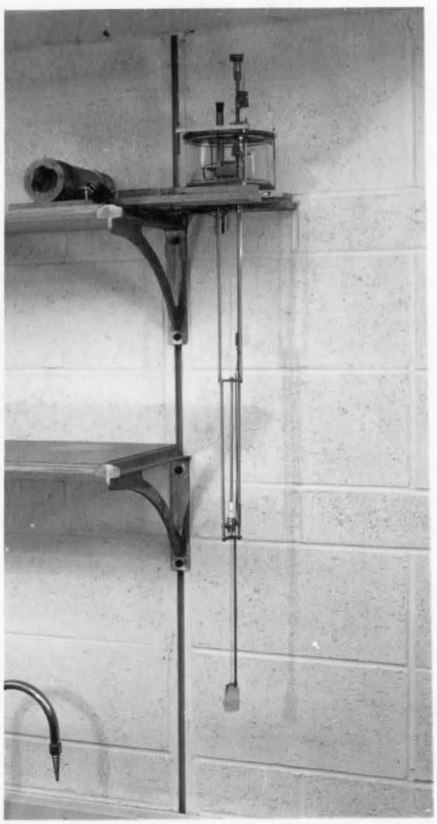

(c)

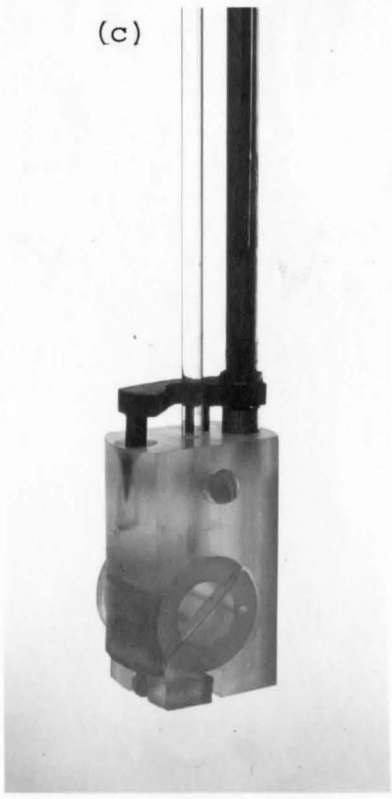

(b)

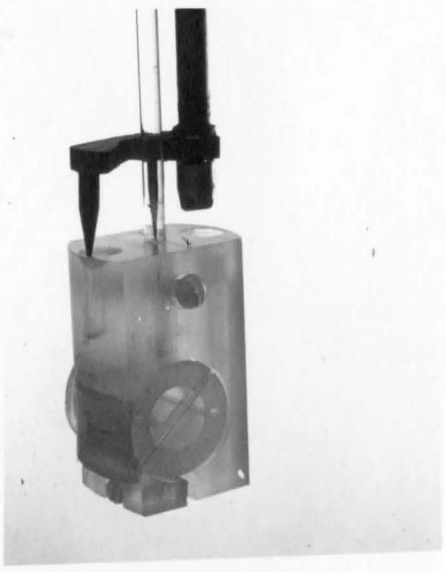

(d)

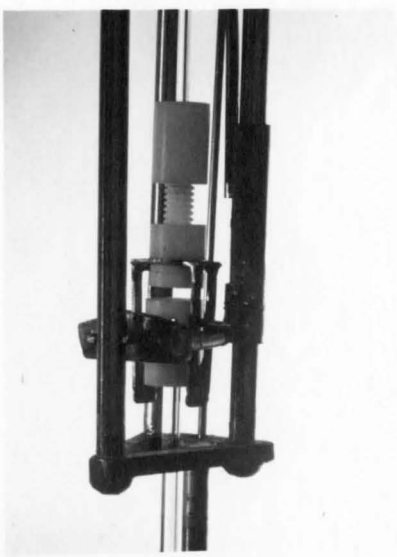

Figure 5

Induced Torque Apparatus

The mercury crystals were grown of 99.99999% pure mercury supplied by United Mineral and Chemical Corporation. The method of growth has been described by Dixon[43]. A keyway was machined into the side of the holder for alignment purposes. The growth tube was cut from the holder leaving a length of sample approximately equal to its diameter.

B. EXPERIMENTAL RESULTS

The sample traces,shown in Figure 6, were recorded using a fast rate of rotation and show the reversal of the torque when the rotation was reversed. The peaks at 20 degrees and at 106 degrees were due to open orbit conductivity. The noise was primarily due to uneven magnet rotation except where the large torque at the strong open orbit has caused the sample to swing on the quartz rod.

The amplitude of a strong open orbit peak was plotted against rotation speed for rates from 0.0016 radians per second to 0.014 radians per second at constant magnetic field. The results agreed with the linear ω dependence of III.8 and III.9 within experimental error, taking into account the one cycle per second response of the amplifier used. The dependence of amplitude on the magnitude of B was not B^2 as indicated in III.8 and III.9 but was B^x, where x varied with B, but generally was less than 2. This implied that σ was still a function of B, as would be expected for a finite $\omega\tau$.

An experimental check of the model was made by W. R.

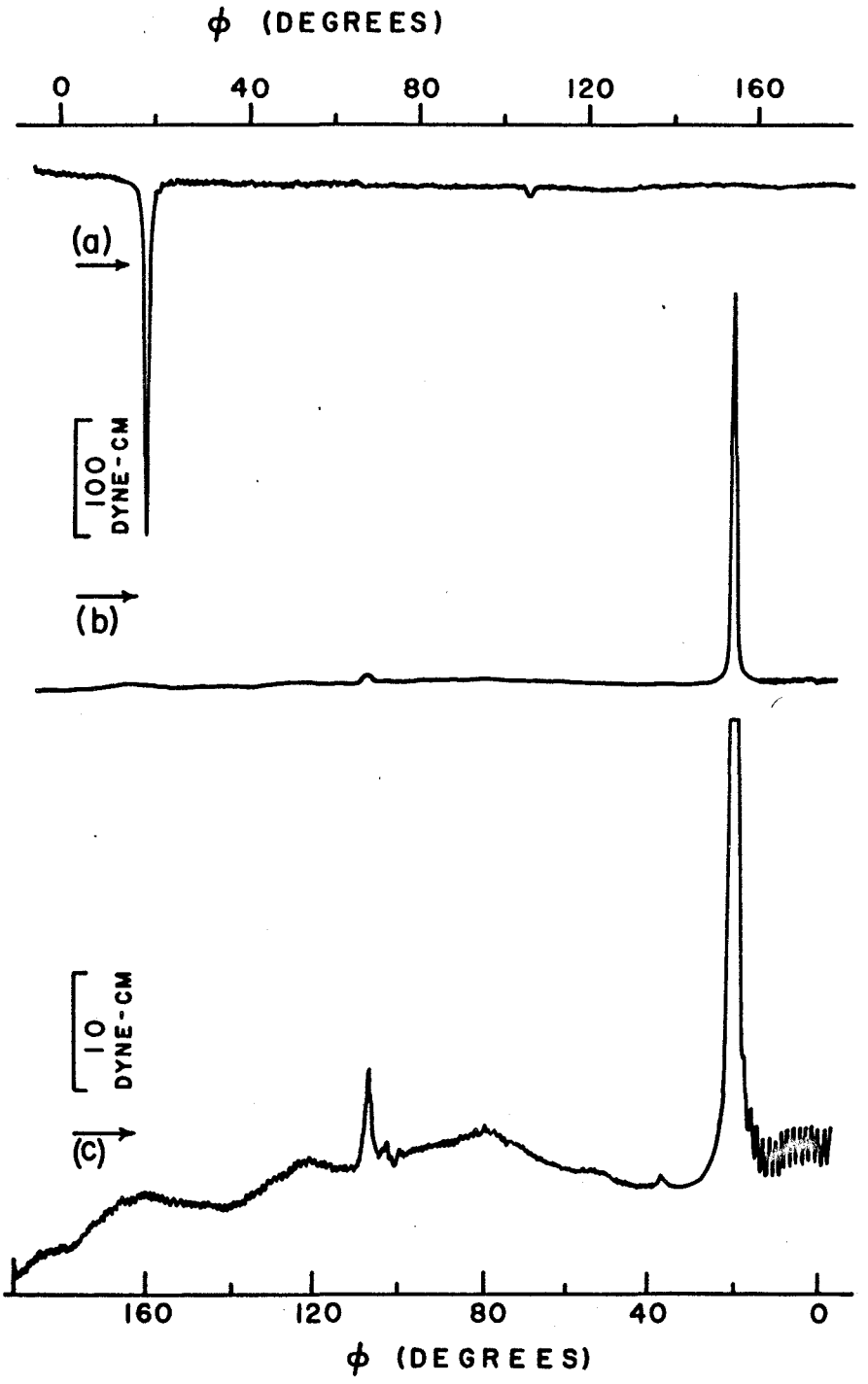

Figure 6

Torque as a Function of Magnetic Field Direction. The magnet rotation was from 0 degrees to 180 degrees for trace (a) and from 180 degrees to 0 degrees for (b) and (c). The sensitivity of the magnetometer was increased 10× for (c).

Datars by measuring the induced torque for a sample of copper. It was found that the torque increased when conditions for an open orbit existed, even though copper is an uncompensated metal. This shows that the torque is dominated by the σ_{yy} term of the conductivity tensor, since the latter becomes large and is independent of B when $\bar{B}$ is perpendicular to the open orbit. This supports the assumption that the Hall terms of the conductivity matrix do not affect the induced torque.

Figure 7(a) shows a stereogram of the positions of the torque peaks obtained for a mercury sample. These peaks agreed well with the open orbit directions of Datars and Dixon[28]. The (001) and $(1\bar{1}0)$ orbits were not observed for this sample as they were along the torque axis when $\bar{B}$ was perpendicular to the orbit. Other small peaks, generally without the shape of an open orbit peak, were also observed, though no peaks were seen corresponding to the (1,2,3) orbits reported in (28). One experiment was continued after the helium bath had dropped below the sample. Although no temperature measurements were made it was noted that the peak lost amplitude and sharpness as the temperature rose, but that, using the same sensitivity, the width of the peak did not change.

Since the height and shape of the torque peaks allowed one to differentiate between large and small changes of conductivity it was possible to distinguish between open

orbits and extended orbits. The conductivity at an open orbit was determined by the mean free path of the carriers as well as their number. Thus, as the field was swept through the plane perpendicular to the open orbit the conductivity increased until it was limited by scattering precisely at the open orbit direction, then decreased again, leaving a sharp peak for a good crystal at low temperatures. An extended orbit did not result in the sharp peak as the mean free path was limited to the extension of the orbit. The maximum torque for each peak from A to A on Figure 7(a) was plotted against angle along the orbit in Figure 7 (b). The small peaks observed for angles from 9 degrees to 18 degrees for the [001] direction were considered to be due to extended orbits rather than open orbits. Magnetoresistance results[28] indicated a range of $\pm$ 18 degrees for this orbit, but gave no information on the magnitude of the conductivity. The $(1,\bar{1},0)$ band of orbits were found to agree well with the angular range as found by magnetoresistance data. The amplitude of the open orbit decreased abruptly at the end of this band and no small peaks were observed. The (1,2,3) orbit was not detected. Also the amplitude of the peak very near the [001] direction was much less than the peak amplitude for each of the open orbits which cross at this point.

C. DISCUSSION

The technique of induced torque allows the determination of open orbit directions in both compensated and uncompensated

Figure 7(a)

Stereogram of magnetic-field directions in reciprocal space of induced torque due to open-orbit conductivity. The pole of the stereogram is along the [111] direction. Point p is the pole about which the crystal was rotated to obtain different orientations relative to the plane of rotation. Directions normal to crystallographic planes are shown.

Figure 7(b)

Relative amplitude of torque for directions in region AA of Figure 7(a) as a function of the angle from the [001] direction.

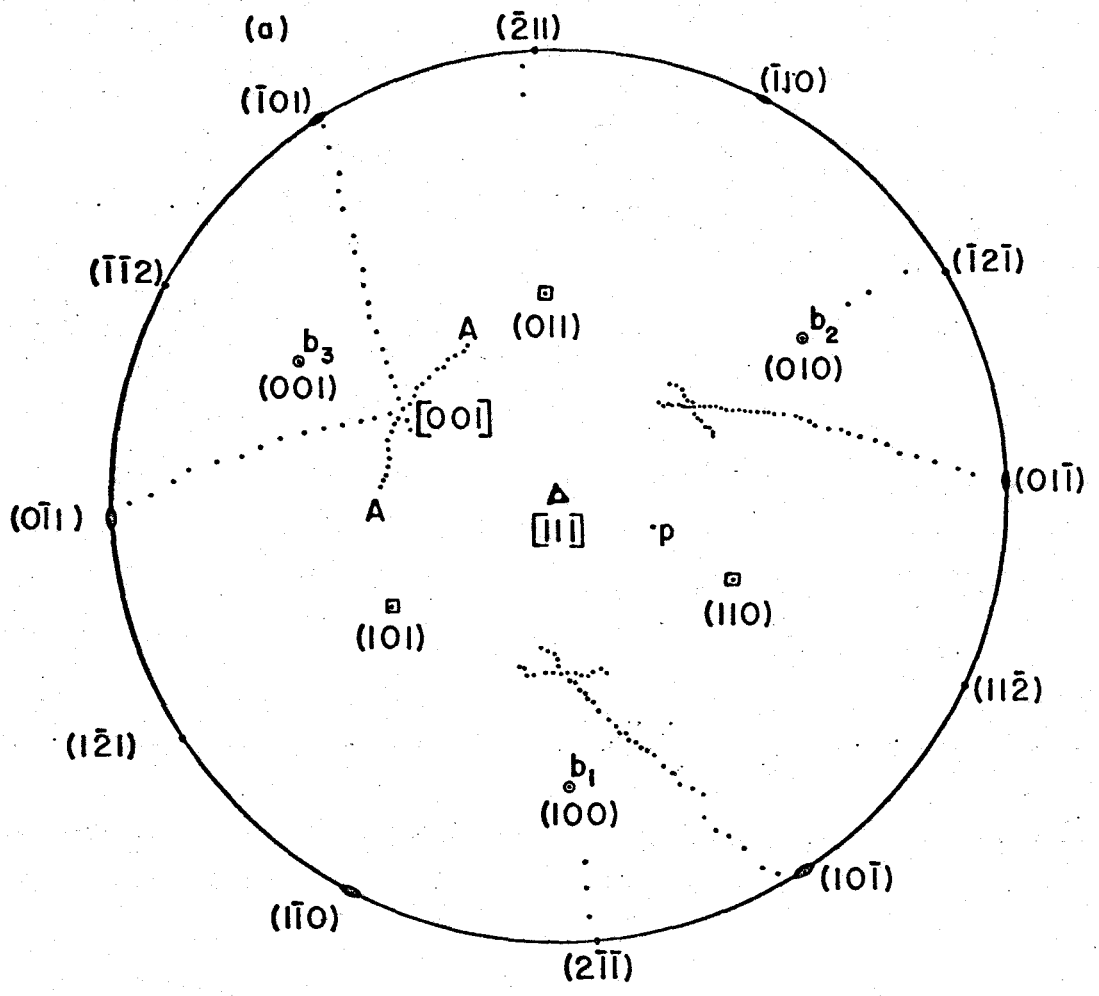

Figure 7(a)

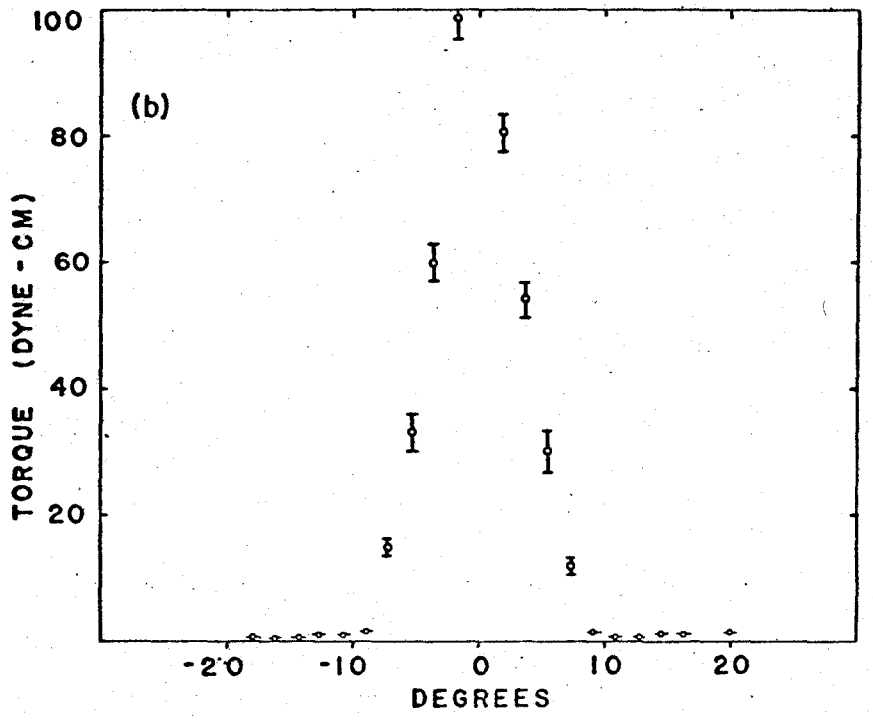

Figure 7(b)

metals. The sample shape is not critical for obtaining signals, although the signal amplitude is not independent of either the sample size or shape. In the usual transverse magnetoresistance geometry there is a cone of solid angle about the current direction in which the magnetic field may not be oriented. This blind spot is removed by the induced torque method. The dependence on the angle between the open orbit direction and the current direction is preserved in this case as is demonstrated by the orbits which are missing in Figure 7(a).

For a sample of regular geometry it is possible to distinguish between orientations which give rise to large, sharply peaked signals due to open orbits and those which result in small, unpeaked signals, probably due to extended orbits.

The method is also useful for orientation of crystals where Laué techniques are inconvenient or where the surface condition of the sample makes such orientation either misleading or impossible. As the effect involves the volume of the sample it can reveal the presence of large crystalites in any part of the sample. From III.8 and III.9 it is seen that the signal increases more rapidly than the volume of the sample.

No contacts on the sample are necessary when using the induced torque method. This obviates the need for leads to the high gain DC amplifier and the resultant voltage pick-

up problems. Although no leads from the sample are required, it is necessary to rotate the sample about a horizontal axis without adding any permanent constraints to the system. The system described in this thesis performs this function but is very sensitive to alignment problems and sensitive to damage.

CHAPTER IV

TEMPERATURE DEPENDENCE OF THE dHvA EFFECT AMPLITUDE

Analysis of the amplitude of the dHvA effect yields the cyclotron mass and the Dingle temperature. Consistent amplitude measurements are made more easily by using the torque method than by using field modulation techniques. The torque is measured by a null method where the nulling current is recorded directly. On the other hand, the signal obtained using field modulation depends on the amplitude of the modulation in the volume of the sample. This depends not only on the current in the modulation coils, but also on the penetration of the modulation field into the sample. In addition, since heat is generated in the sample by the modulation, there is considerable difficulty in maintaining and measuring the sample temperature, particularly above the λ-point. The amplification of the signal depends on the gain, frequency, and phase adjustments of the phase sensitive detection system. The signal to noise ratio, due to the β arms, was found to be several times larger for the torque method than for the field modulation method. Thus if large torque oscillations are obtained for the desired carrier, as was true in this case, the torque method is preferred for amplitude measurements.

The sinh and Dingle temperature factors in II.38

may be approximated by

$$e^{\frac{-2\pi^2 sK(T+T_D)}{\hbar\omega_c}}$$

where $T_D = \frac{\hbar}{2\pi^2 K\tau}$.

Since τ is limited by both impurity and phonon scattering, T_D may be expressed as $T_D = CT^n + D$ where CT^n, the phonon term, depends on the temperature. The constant term D is due to scattering by static lattice imperfections. Dingle[18] has shown that the term D is expected to be much larger than the term C. If this prediction is not true it should be possible to observe the effect in mercury, due to its low Debye temperature. Provided the index n is not equal to or less than unity, the plot of ln (amplitude/T) against T will show a negative curvature. A value of n below unity is very unlikely.

A. EXPERIMENTAL CONSIDERATIONS

The magnitude of the torque dHvA effect as a function of temperature and magnetic field was measured accurately. A single β arm frequency for a magnetic field direction 24 degrees from the minimum frequency in the trigonal-bisectrix plane was used. This orientation was chosen because there was little interference from other oscillations. The apparatus was similar to that used for the torque open orbit experiment described in the previous chapter with the exception that there was no facility for rotating the sample aboutan horizontal axis.

Two traces, one each for increasing and decreasing field, were recorded for each temperature. Field markers were put on the trace automatically using a modified Rawson rotating coil gaussmeter. The accuracy of the markers was $\pm$ 5 millitesla over the range from 1.4 to 2.3 tesla. The sweep rate was sufficiently slow that the one cycle per second response time of the recording system did not affect the amplitude. At the higher temperatures and lower fields, noise on the traces limited the accuracy of the amplitude measurements to several percent. For the other readings the accuracy was limited by reading errors of less than one percent.

The predominant source of error occurred in the temperature measurements,which were obtained by measuring the pressure above the bath. Errors arose from a lack of static equilibrium between the bath and the sample, from the assumption that the vapour pressure at the helium surface was the measured pressure, and from reading errors in the pressure measurement.

These three sources of error in the temperature measurement varied in importance for different temperatures. Approximately one half hour was allowed after a pressure was attained to permit the sample and bath to reach equilibrium. All readings above the λ-point were recorded after a lowering of the temperature. Some traces were taken below the λ-point after increases in temperature. The amplitudes recorded for some of these readings, taken at the end of the experiment, were less than the amplitudes recorded during the lowering of

the temperature. This showed that the measured pressure no longer indicated the sample temperature, due to the low liquid helium level. This amplitude drop was not caused by lack of equilibrium, which would have caused an increase in the amplitude. Readings showing this lack of temperature equilibrium were not used. The pressure was measured using oil and mercury manometers connected to a thin-walled stainless steel tube of 3/8 inch diameter which was lowered to within a few inches of the helium surface. An Autovac vacuum gauge, using a pumping line correction and the manufacturer's calibration for helium, was used to verify the manometer readings. Agreement within experimental error between the manometer and Autovac gauge was obtained. The error in the temperature measurement was estimated at $\pm$50 $m^{o}K$ for the least accurate measurements, which occurred in the region above the λ point, while $\pm$ 20 $m^{o}K$ was estimated for the temperature readings below the λ-point

B. ANALYSIS OF THE dHvA TORQUE AMPLITUDES

The amplitude measurements were used to determine the cyclotron effective mass, m_c, and the Dingle temperature, T_D from II.38. It was possible to place limits on the constancy of these quantities for the magnetic field and temperature ranges used.

The data obtained, shown in Table I, were plotted on a semilog graph to determine an approximate value of m_c using the method outlined by Berlincourt[44]. Plotting

TABLE I

Amplitude of Torque of dHvA Oscillations (mV)

Temp (^{o}K)	Magnetic Field (tesla) 1.3	1.4	1.5	1.6	1.7	1.8	1.9	2.0	2.1	2.2	2.3
4.23		0.71	0.27	0.40	0.66	1.20	1.77	2.64	3.50	5.50	6.7
3.75			0.50	0.79	1.30	2.05	2.90	4.12	5.60	7.53	9.75
3.10		0.71	0.98	1.8	2.78	3.83	5.18	7.13	9.45	12.5	15.8
2.18			3.14	5.0	7.16	9.88	12.7	15.9	20.3	25.3	30.9
1.76			5.6	8.3	11.2	14.8	18.7	23.1	28.3	34.3	40.9
1.53	2.8	4.7	7.0	9.9	13.2	17.3	21.3	26.3	31.7	38.0	45.0
1.47	3.2	5.1	7.3	10.3	14.0	17.9	22.2	27.1	32.9	39.4	46.3
1.30	4.1	6.2	9.0	12.2	16.2	20.6	25.1	30.4	36.5	43.6	50.6
1.23	4.4	7.0	9.6	12.8	17.0	21.6	26.2	31.4	37.8	45.0	51.9
1.25	4.4	6.8	9.4	12.7	16.8	21.3	25.9	31.1	37.3	44.5	51.7
1.27	4.2	6.6	9.1	12.4	16.5	21.1	25.8	30.9	37.3	44.4	51.8

TABLE II

Cyclotron Effective Mass

B (tesla)	$\frac{m_c}{m_o}$
2.3	0.180
2.2	0.180
2.1	0.179
2.0	0.180
1.9	0.179
1.8	0.178
1.7	0.173
1.6	0.170
1.5	0.180

TABLE III

Dingle Temperatures

Temp. (^{o}K)	T_o (^{o}K)
4.23	2.42
3.75	2.24
3.10	2.36
2.18	2.56
1.76	2.50
1.53	2.52
1.47	2.52
1.25	2.45

ln (amplitude/T) against temperature was equivalent to approximating the $\{\sinh[+2\pi^2 KT/\beta B]\}^{-1}$ factor in II.38 by $\exp[-2\pi^2 KT/\beta B]$ where $\beta = \frac{e\hbar}{m_c}$. The value of m_c obtained from the slope was used to plot $\ln[(\text{amplitude})T^{-1} \exp\{-4\pi^2 KT/\beta B\}]$ against temperature in order to obtain a second approximation to m_c. The sinh corrections never exceeded 4% of (amplitude/T). A slight positive curvature, of about the same size as the error, still existed in the corrected plots of the data recorded at higher magnetic fields.

The cyclotron effective mass, m_c, was determined for several magnetic field values, as shown in Table II. In terms of m_o, the free electron mass, the average cyclotron effective mass determined from these plots is

$$m_c = 0.178 \pm 0.02\ m_o. \qquad \text{IV.1}$$

The error includes the scatter of the elements of Table II as well as the curvature of the plot. The predominant error was random, and no definite dependence of m_c on field or amplitude was found. Thus m_c was constant within this error over temperatures from 1.25°K to 4.2°K and fields from 1.5 tesla to 2.3 tesla.

The term $e^{\frac{-s}{\omega_c \tau}}$ of II.38 was expressed in terms of the Dingle temperature $T_D = \frac{\hbar}{2\pi^2 K\tau}$. T_D was calculated from the slopes of the plots obtained when

$$\ln\{(\text{amplitude})\ B^{3/2}[1 - \tfrac{4\pi^2 KT}{\hbar\omega_c}]\}$$

was plotted against B^{-1} for certain temperatures from 1.25°K to 4.2°K. The plots were linear within experimental error, and yielded the Dingle temperature values shown in Table III. The average value was

$$T_D = 2.4 \pm 0.1^{\circ}K \quad . \qquad \text{(IV.2)}$$

which was indicative of a somewhat imperfect crystal. The error was random and indicated that the Dingle temperature was independent of temperatures from 1.25°K to 4.2°K and of magnetic fields from 1.5 tesla to 2.3 tesla to within ± 4%.

The slight positive curvature still existing in the plots of

$$\ln\{(\text{amplitude})\ T^{-1}\ \exp[-4\pi^2 KT/\beta B]\}\ \text{vs}\ T$$

was of the order of the scatter on the data points. This curvature, although certainly not large enough to justify invoking a mechanism to explain it, does eliminate the possibility of a negative curvature in these plots. There are, however, several effects which could affect the dHvA amplitudes, and thus the analysis which led to II.1 and II.2.

One of these, the electron-electron interaction, may reduce the discontinuity in the Fermi function at the Fermi surface to some fraction of that predicted for non-interacting particles. This modification will not affect the temperature dependence of the dHvA effect amplitude, merely scaling all the amplitudes by a constant fraction. Luttinger[45] has shown that this effect cannot change the temperature or field dependence of the amplitude.

The other effect which could have changed the tempera-

ture or field dependence of the amplitudes is related to the harmonic content of the oscillations. There are two sources of harmonic content which affect the amplitudes of the dHvA oscillations. These were the harmonic terms of II.38 which became important for low temperatures and high magnetic fields, and the harmonics due to magnetic interaction and magnetometer compliance effects. Since it was the envelope of the oscillations which was measured, it was necessary to evaluate the envelope amplitude in terms of the amplitudes of the harmonics.

To evaluate the effects of the dHvA harmonics the first two terms of II.38 were retained. The resultant equation, divided by the amplitude of the fundamental, is of the form

$$A = \sin \phi - b \sin 2\phi \qquad \text{IV.3}$$

where $\phi = \frac{\hbar A_o}{eB}$ and b is the ratio of the amplitude of the second harmonic term to the amplitude of the fundamental. The expression for b,

$$b = (\tfrac{1}{2})^{\frac{1}{2}} \exp\left\{\frac{-2\pi^2 K(T+T_D)m_c}{e\hbar B}\right\} \frac{\cos(\frac{\pi 2gm_c}{2m_e})}{\cos(\frac{\pi g m_c}{2m_e})} ,$$

was evaluated for a temperature of $1.3^{o}K$. The values ranged from b = 0.0007 for B = 1.6 tesla to 0.005 for B = 2.3 tesla. In order to find the relation between b and the envelope amplitude, which was measured, the trigonometric functions of IV.3 were expanded about the minimum and maximum values of sin ϕ. Differentiation to find the extrema of IV.3 gave

$$A = 1 + 2b^2 \qquad \text{IV.4}$$

Thus the increase in the envelope amplitude due to the second order term of II.37 was less than 0.01% at the lowest temperature and highest field used. Since the harmonics higher than the second were smaller yet, the increase in the envelope amplitude due to the higher order dHvA harmonics was negligible.

The harmonic content from either magnetic interaction or magnetometer compliance effects have been shown by Vanderkooy[40] to take the form

$$\frac{y}{a} = (1 - \frac{a^2}{8}) \sin\phi - \frac{a}{2} \sin 2\phi + \frac{3}{8} a^2 \sin 3\phi. \qquad \text{IV.5}$$

$\frac{y}{a}$ corresponded to A in IV.3 and a indicated the amount of interaction, either magnetic or mechanical. Again it was possible to obtain the relation between the envelope amplitude and the coefficients in the harmonic expansion. When IV.5 was expanded about the extrema of sin x and differentiated it was found that

$$A = 1 - 2a^2 + \text{higher terms.} \qquad \text{IV.6}$$

First it is noted that this term can only result in a reduction of the envelope. Also the coefficient 'a' was reduced by using a stiff torque suspension. The precautions which were taken to reduce the torque compliance have been described by Vanderkooy[40]. Oscillations of as low frequency as those used in this study were not expected to exhibit detectable magnetic interaction. Thus the term $-2a^2$ was negligible.

It is seen that no detectable modifications were found to equation II.38 due to harmonic effects. As indicated

earlier no modification is expected to arise from the electron-electron interaction. Thus no reason was found to doubt the values of m_c and T_D.

Within the limits of error it was found that there were no effects on either the cyclotron effective mass or the Dingle temperature to suggest modification by real phonons. The virtual phonon contribution to the effective mass would be included in the cyclotron mass detected in this experiment. Because the spacing of the Landau levels, and thus the mass, was measured by their relation to the Fermi-Dirac distribution function, effects due to temperature dependent scattering would have been visible, as they broaden the levels. As outlined at the beginning of this chapter the Dingle Temperature $T_D \propto 1/\tau$ may be expressed as CT^n+D with C and D being constants. An attempt was made to set a lower bound on n by measuring the transverse magnetoresistance of a mercury sample as a function of temperature. In this case n was found to be approximately 2. Thus n was expected to be significantly larger than 1 in the case of the de Haas-van Alphen effect. The absence of a further reduction of the amplitude at higher temperatures indicated that C was small as compared with D. Therefore, as predicted by Dingle[18], no phonon effects were observed in mercury.

CHAPTER V

THE MODULATION TECHNIQUE

Differential field modulation techniques (F.M.T.) were used to study some of the closed orbits of mercury. The geometry used involved modulation and detection coils where the coil axes were colinear with the applied field $\bar{B}$. Goldstein, Williamson and Foner[46] have described a method, which they credit to Dr. Hernan Praddaude, for obtaining higher derivatives of the magnetization and for discrimination against certain dHvA frequencies.

The modulation may be expressed as

$$B = B_o + B_M \cos \omega t \qquad V.1$$

where $B_o >> B_M$. If II.40 is written as

$$m = m_o (B) \sin \left(\frac{\hbar A_o}{eB}\right) \qquad V.2$$

then $m_o(B)$ is the slowly varying amplitude of $\sin \left(\frac{\hbar A}{eB}\right)$ and the phase in the argument has been ignored along with the higher harmonics. With the aid of V.1, V.2 may be approximated by

$$m = m_o(B_o) \left\{\sin\left(\frac{\hbar A_o}{eB_o}\right) \cos(\alpha \cos\omega t) - \cos\left(\frac{\hbar A_o}{eB_o}\right) \sin(\alpha \cos\omega t)\right\} \qquad V.3$$

where

$$\alpha = \frac{\hbar A_o B_M}{eB_o^2} .$$

Expansion of V.3 in harmonics yields

$$m = 2m_o(B_o)\{\sin(\frac{\hbar A_o}{B_o e})[\frac{J_o(\alpha)}{2} + \sum_{n=1}^{\infty}(-1)^n J_{2n}(\alpha)\cos 2n\omega t]$$

$$-\cos(\frac{\hbar A_o}{B_o e})[\sum_{n=0}^{\infty}(-1)^n J_{n+1}(\alpha)\cos\{(2n+1)\omega t\}]\} \quad V.4$$

where $J_n(\alpha)$ is the n'th order Bessel function.

It may be seen that any single oscillation can be eliminated or maximized by maintaining α such that a particular Bessel function is made zero or maximum. If $\alpha << 1$ then the Bessel functions may be approximated by

$$A_n = 2(\frac{\alpha}{n})^n \frac{\partial^n(\frac{\hbar A_o}{eB_o})}{\partial B_o^n} .$$

Thus the amplitude of the n'th harmonic of the modulation frequency is the n'th derivative of the argument of the dHvA oscillation.

The technique of maintaining α constant by varying B_M as B_o^2 was not used in this experiment as modulation of sufficient magnitude to be useful caused the magnet to go normal. However, the method of obtaining higher frequencies by means of detecting the higher harmonics of the modulation was employed extensively with considerable success.

A. THE FIELD MODULATION TECHNIQUE APPARATUS

The magnet used to perform the field modulation measurements was a Westinghouse superconducting solenoid with a 1.00 inch inside diameter and field uniformity of

1×10^{-4} in a 0.5 inch sphere. The coil consisted of 66,813 turns, plus two end correction coils of 1,252 turns, each of 0.010 inch niobium base alloy wire (niobium zirconium). The wire was plated with copper and enamelled. The rated field of 55,000 oersteds and the homogeneity were tested and found to be within the specifications.

The diameter of the inner dewar was 0.812 inches. The experimental apparatus was situated within this diameter with the exception of a coil of number 40 enamelled copper wire which was wound on the outside of the inner dewar. This coil was used at various times for modulation and as a sweep coil for obtaining linear magnet sweeps.

The usual method of sweeping was to maintain the voltage across the magnet constant. This resulted in a sweep which was linear to about 10% at the beginning of a trace. However, after the first thousand oersteds of sweep, the sweep rate was much more constant. Since extremely linear sweeps were not necessary in this work, the rate coil and current regulated modes of sweep were seldom used. The power supply has been described by Vanderkooy[40].

The apparatus used to orient the sample and support the modulation and pickup coils is shown in Figure 8. The primary material was kel-F with a nylon monofilament belt to turn the lower drum and nylon screws to secure the ends of the belt. The modulation coils were each about 200 turns of number 34 copper wire while the pickup coils were composed of

CUTAWAY VIEW OF FIELD MODULATION DHVA APPARATUS

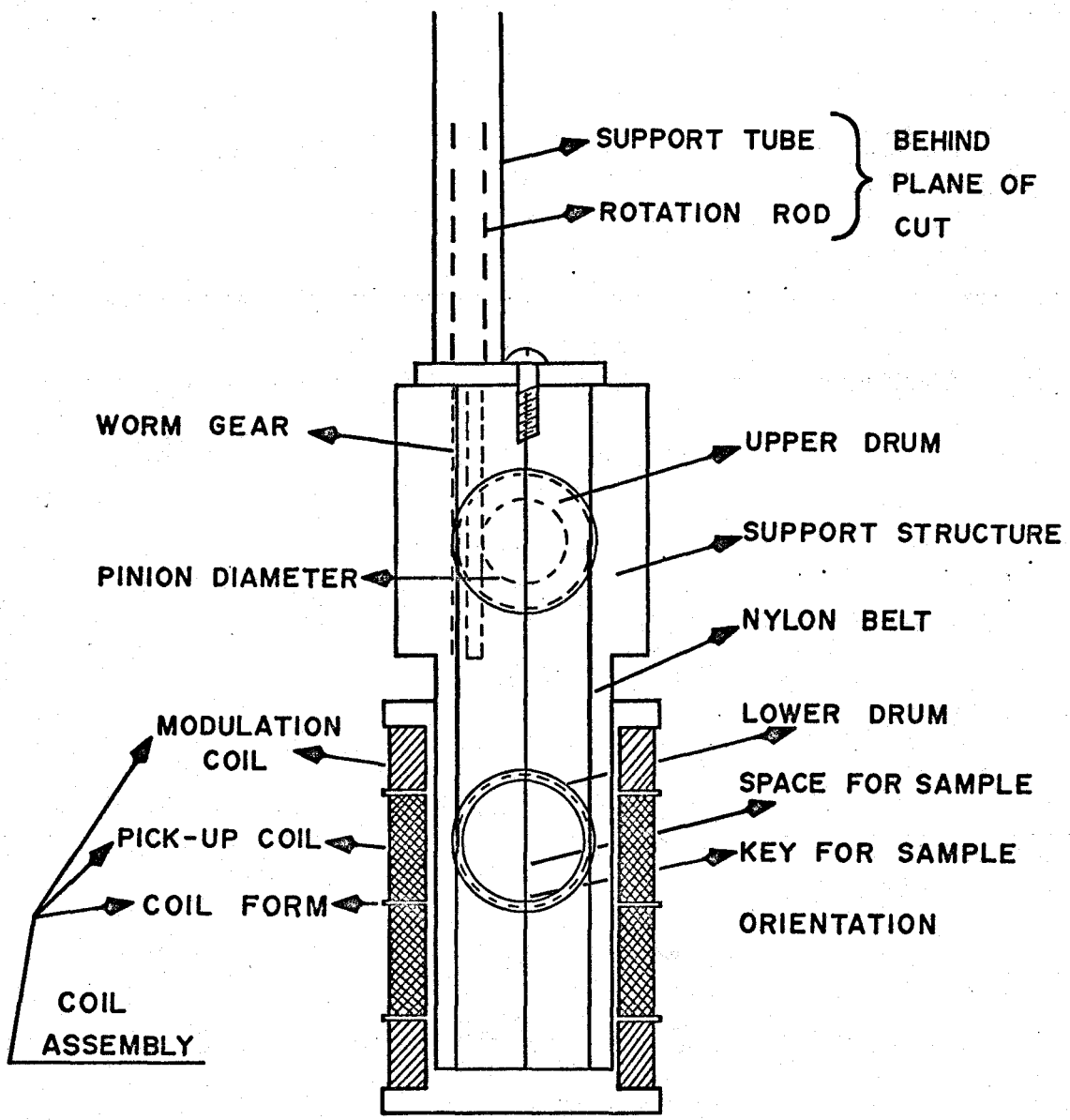

Figure 8

4000 turns of number 44 copper wire. These coils were wound on a teflon bobbin which was a shrink fit onto the centre cylinder, as the coefficient of expansion is greater for teflon than kel-F. The sample was placed in the hollow driven cylinder in the upper coils, the coil bobbin installed and the apparatus inserted in the inner dewar. The turns ratio was such that 44 turns of the worm gear gave 360 degrees of sample rotation.

Orientation of the sample was accomplished using back reflection Laué techniques at liquid nitrogen temperatures[43]. To shorten the exposure time the liquid nitrogen was allowed to fall below the sample. This was possible because some surface frost was permissable. Since the range of possible incident and reflected x-ray angles was restricted by the kel-F holder it was possible to determine the direction of only one symmetry axis from the symmetry of the Laué photograph. Directions relative to this axis were determined by an analysis of the spacings of the spots along a symmetry plane.

For the F.M.T. experiments a 0.400 inch cylinder was bored and drilled to accept an index pin such that the desired crystal axis was directed along the horizontal axis of rotation of the apparatus shown in Figure 8. The net error in the alignment accuracy was of the order of 5 degrees.

A block diagram of the detection and recording system is shown in Figure 9. The output of the modulation amplifier

BLOCK DIAGRAM FOR F.M.T.

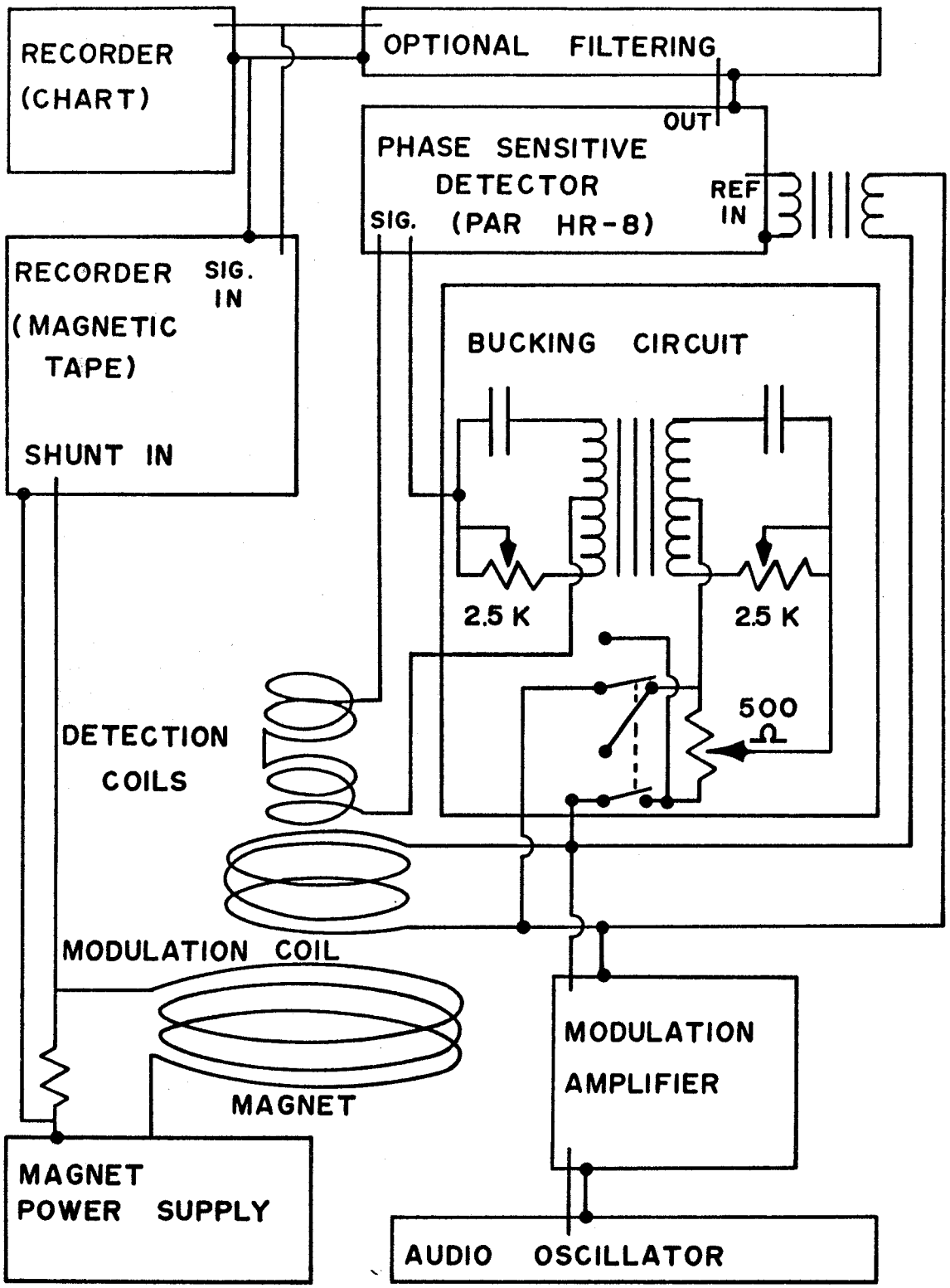

Figure 9

was stabilized to compensate for gain changes and changes of the oscillator output voltage. Because of strong inductive coupling between the modulation coils and the magnet, the modulation frequency was maintained at 400 Hz. Higher frequencies required severe reduction of the modulation amplitude to maintain the magnet in the superconducting state. 10 to 20 millitesla as much as doubled the helium boil-off from each dewar at 400 Hz, thus limiting each run to approximately six hours without retransferring into the inner dewar.

A Princeton Applied Research Lock-in amplifier, PAR, was used in the select external mode to phase sensitively detect the difference signal from the detection coils. A nonlinear circuit, not shown in Figure 9, generated harmonics for the external reference signal when detection was performed at harmonics of the modulation frequency. Detection frequencies up to 1600 cps were found to be useful. In order to prevent saturation of the PAR input preamplifier due to the large 400 cps background signal, a portion of the amplifier output was phase shifted and subtracted from the signal.

The output of the PAR was filtered, if necessary, and recorded. A 12 db/octave low pass filter, incorporated in the PAR, was necessary to remove high frequency noise, effectively reducing the amplifier AC bandpass to approximately 1 cps at 400 cps. To reduce background drift a high pass filter with a response time of 20 to 60 seconds was used.

Hand analysis was simplified by a narrow band twin-T filter of variable Q which reduced the amplitude of neighbouring signals relative to the desired frequency. Q's from 2 to 20 were found most useful, although the narrow band characteristics of the noise passed by a high Q filter was found to be misleading.

Traces to be hand analyzed were recorded on a Moseley strip chart recorder along with field markers, accurate to $\approx .5\%$, and obtained from a magnet current shunt. Oscillations were counted and the beats analyzed to obtain up to three frequencies per trace.

Fourier analysis methods, requiring hundreds or thousands of samples of the signal amplitude and field readings of relative accuracy to 0.01%, were made possible by the use of a digital magnetic tape recording system.

B. THE DATA ACQUISITION SYSTEM

A data acquisition system was used to record some of the field modulation results. This system was a recording voltmeter. Voltages proportional to the field and signal amplitude were alternately recorded on magnetic tape. A block diagram is shown in Figure 10.

The channel selector alternated the input of the DVM between the two inputs by means of mercury wetted relays at rates up to approximately 8 pairs per second. The circuit for the channel selector is shown in Figure 11. The clock frequency was held stable by the use of a zener diode on the

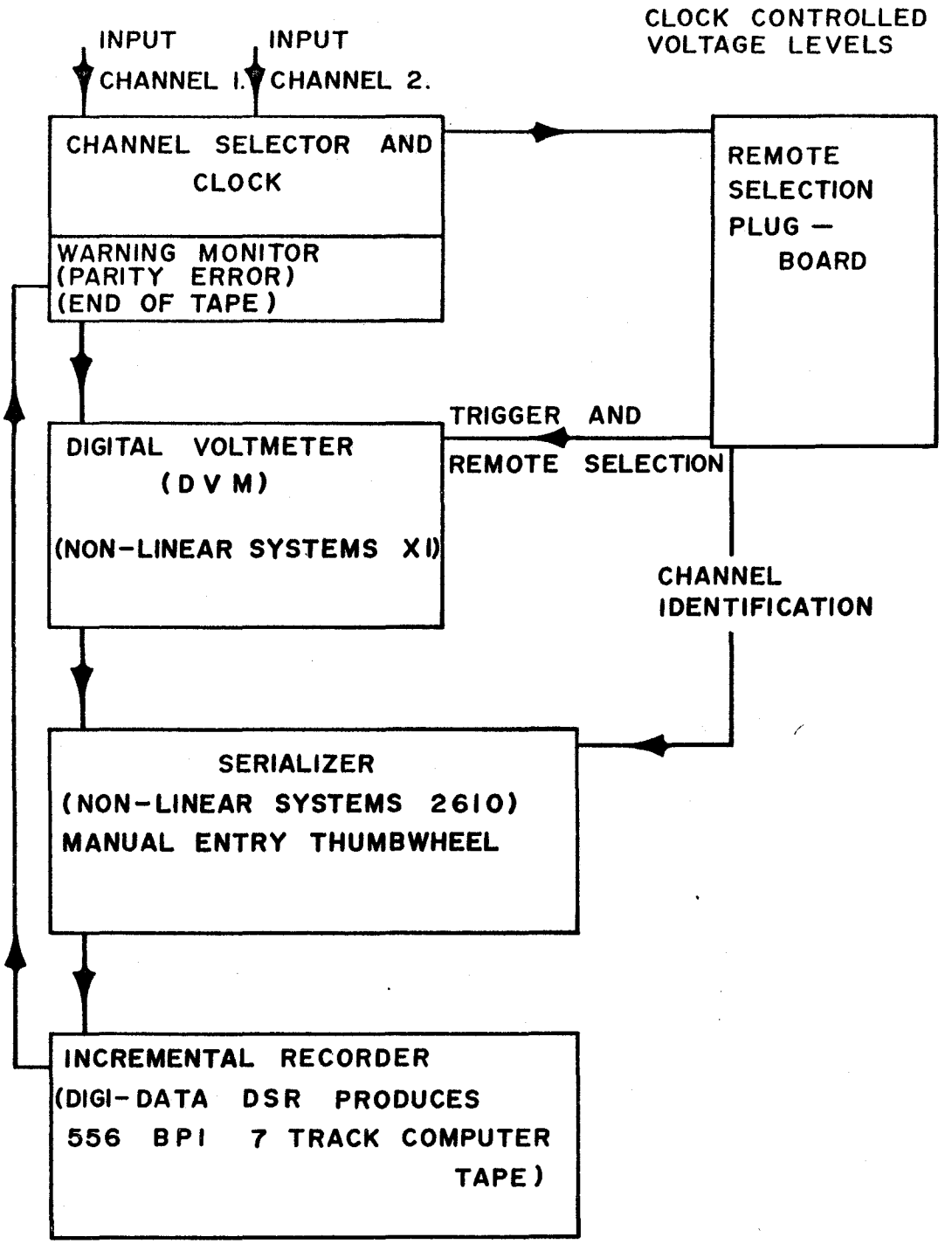

BLOCK DIAGRAM OF DATA ACQUISITION SYSTEM

Figure 10

All resistors are in
K Ω and capacitors in
μf unless otherwise
stated

$Q_{1,2,3,4,5,6,7,8,9,10,13,14,16,17,18,19,21,22,23}$ are 2N1305

Q_{20} is 2N278

$Q_{11,12,24,25,26,27,28,29,30,31,32,33}$ are 2N3705

All diodes silicon, 500 ma

C_1 and C_2 are: 0.5 ; 1.5 ; 4 ; 8 ; 16 ; 32

C_3 is: 0.01 ; 0.022 ; 0.1 ; 0.25 ; 1

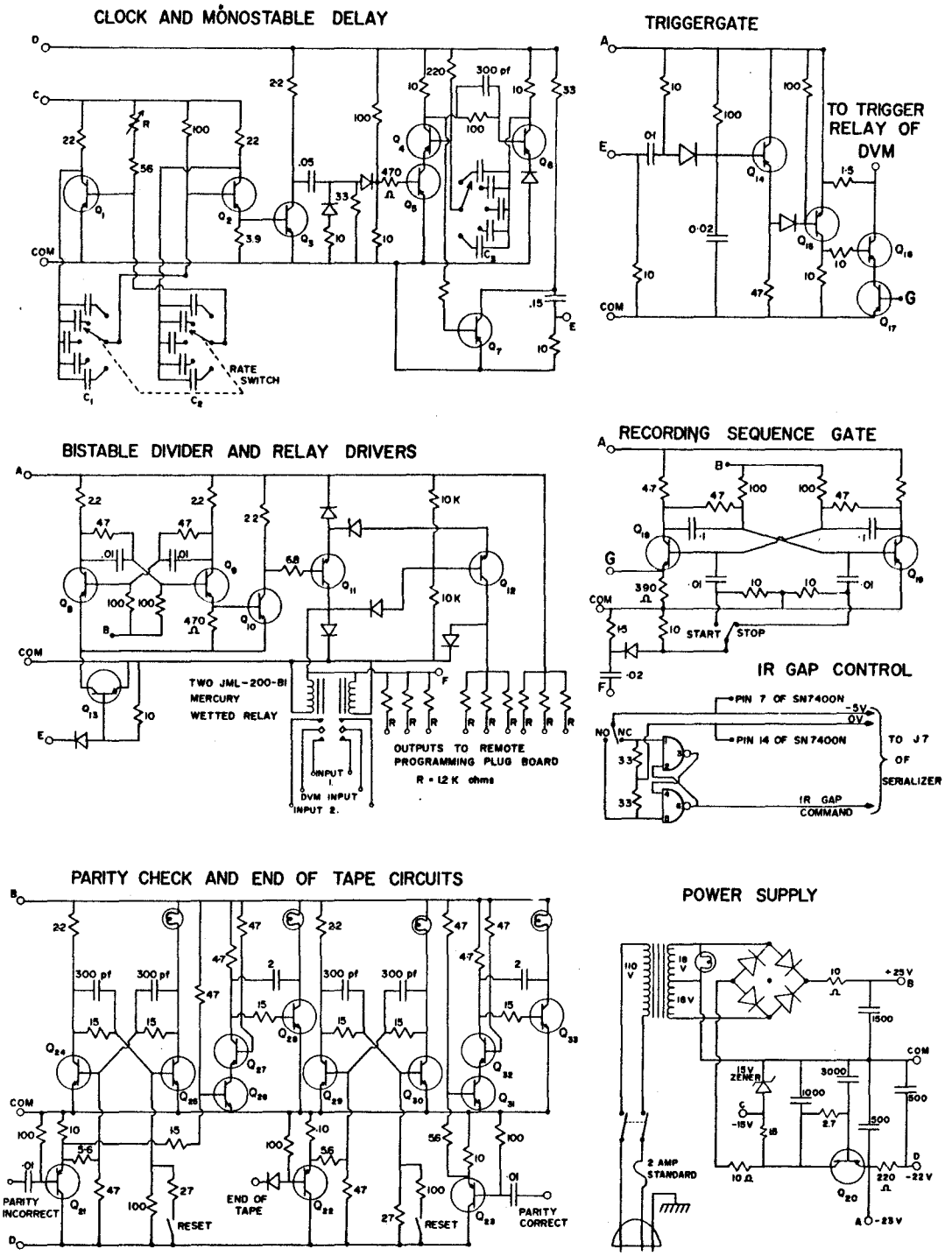

Figure 11

Channel Selector Circuit

supply and the buffer stage Q_3. This frequency was set by the resistor R and the ganged capacitors C. The output of the buffer stage was differentiated, the positive going edge being used to trigger the monostable delay. The output of this delay was differentiated to produce negative and positive going signals. The first pulse was used to switch the bi-stable frequency divider,which in turn drove the input channel selection relays and the digital voltmeter remote selection relays. In this way the alternate readings were taken at equal intervals of time.

Starting with input channel one and ending with channel two was accomplished by means of the trigger gate and the gate control bistable. Pulses derived from the trailing edge of the monostable delay output fired the trigger relay in the digital voltmeter, starting with the first channel one input after the start switch was turned on. The record was terminated with the first channel two reading after the start switch was turned off.

Parity errors, a parity correct signal and the end of tape were indicated by lights on the front panel.

The remote selection plug board allowed programming of the remote selection options of the digital voltmeter. Thus the input range, filtering and polarity could be chosen for each input source.

The serializer, besides providing parallel to series conversion and storage of the data, was equipped with a six

BCD character thumbwheel input for the production of manual identification records. The source of each input voltage could be placed in the channel identification section of each reading.

The incremental recorder produced a 556 bpi, 7 track BCD computer tape which was read by an IBM 7040 computer. The recorder allowed manual entering of inter-record gaps and end of file marks.

The format of the tape was a manual record followed by one or more data records, each record being terminated by an inter-record gap. This was repeated for each trace recorded and the end of used tape was indicated by an end of file mark. The manual records consisted of 18 characters in the form:

|19YYMM|DDPPEE|IIIISS|

where Y denoted the year

M denoted the month

D denoted the day

P denoted the person

E denoted the type of experiment

I denoted characters to be used by experimenter

S denoted sequence number of trace.

Unused fields had to be included as zeros because less than 18 characters was considered to be a noise record by the computer. Each data reading consisted of 12 BCD characters of the form:

YYY FPxxxxxxZ

where YYY denoted a channel number

F denoted function

P denoted polarity

x denoted digital voltmeter reading

Z denoted the range.

Each pair of readings consisted of two of the above forms, or four 7040 words. The first channel number of a data record could never begin with "19" and the number of pairs of readings between two inter-record gaps was limited to 3000.

Four programs were written in MAP by Mrs. S. A.Moss to handle the data[47]. The programs DA1 and DA3 were used to create and maintain binary data files on tape. DA2 was a subroutine used for reading these binary tapes. The information contained in the manual record was included with the binary data and was used to select the blocks of data to be used. The program DA4 was used for error recovery. In this program records were read, error returns ignored if possible, and the records chosen were printed, and, optionally, punched on cards. A full description of these programs may be found in the documentation supplied with them.

The data from a given trace was pre-smoothed by means of another program, DA9, written by Mrs. Moss and using the parabolic fit section of John Jones' fourier analysis program. DA9 allowed removal of specified blocks of data from

the complete recording for that trace. It then subtracted the least mean square parabola from the remaining data points and the smoothed data was written onto a disk file for use by the fourier program.

Two versions of the fourier program were used. Both divided the data into sections by fitting variable length parabolas, then fourier analyzing the parabola for its sine and cosine components for a range of frequencies. These components were summed as each parabola was treated and then the power spectrum was calculated from the components. The first version used was written by J. C. Jones[48] and it calculated a linear average of three field inputs on either side of each amplitude input. The later version, derived from the first by Mrs. Moss, allowed linear smoothing by any number of points, as well as economies of core and time.

The results were plotted on the Benson-Lehner plotter. The program DA5 was written to prepare the tapes required by the plotter. A series of error recovery and editing programs were written to bypass physically unreadable records and to write file marks in certain situations.

C. DESCRIPTION OF THE FIELD MODULATION TECHNIQUE RESULTS FOR MERCURY

Data were recorded for the trigonal-binary and trigonal-bisectrix planes of mercury. These data, analyzed by hand, are shown in Figures 12 and 13. The trigonal-bisectrix plane was repeated; the data, recorded on magnetic tape, were

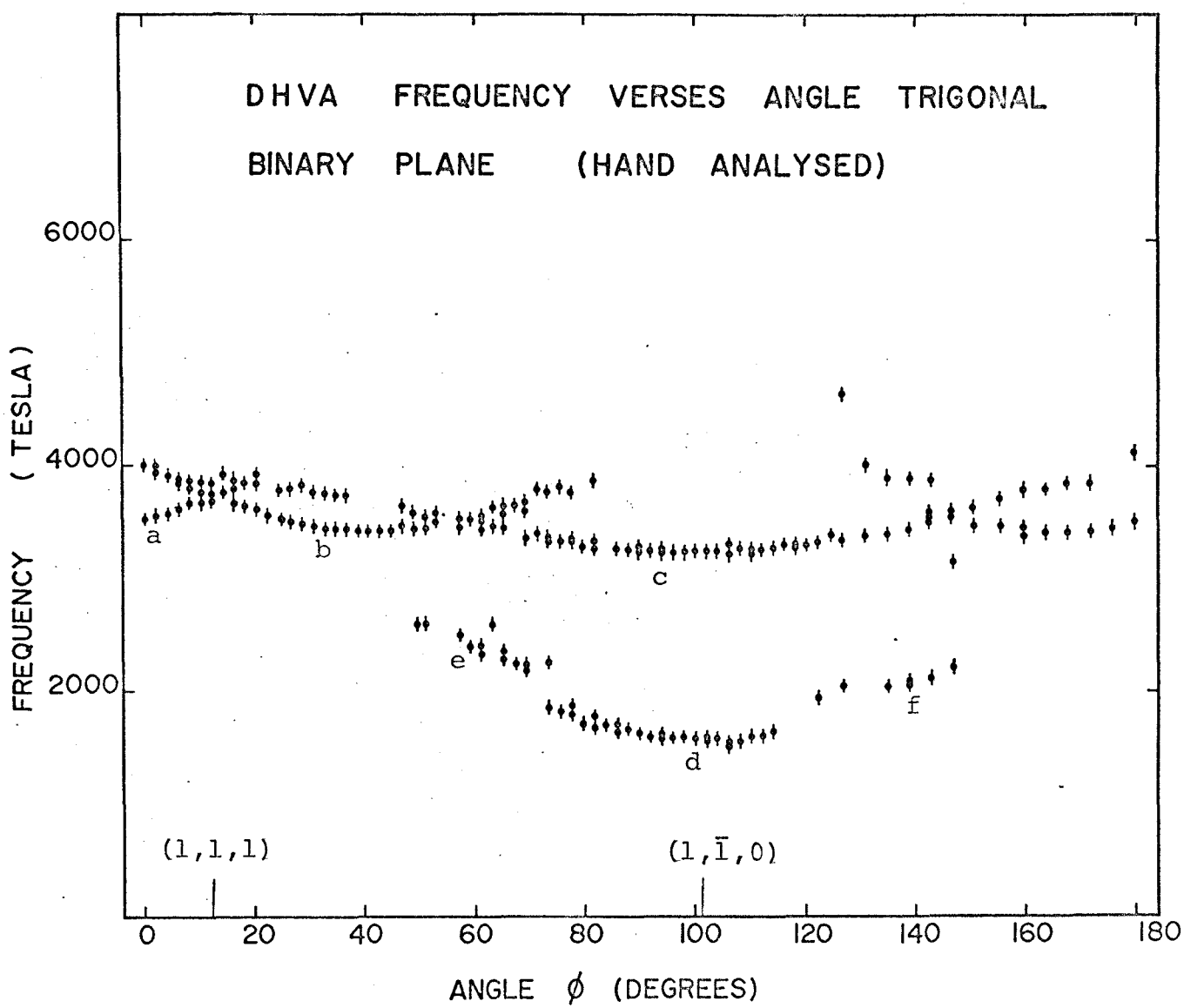
DHVA FREQUENCY VERSES ANGLE TRIGONAL
BINARY PLANE (HAND ANALYSED)
FREQUENCY (TESLA)
6000
4000
2000
a
b
c
d
e
f
(1,1,1)
(1,$\bar{1}$,0)
0
20
40
60
80
100
120
140
160
180
ANGLE ϕ (DEGREES)

Figure 12

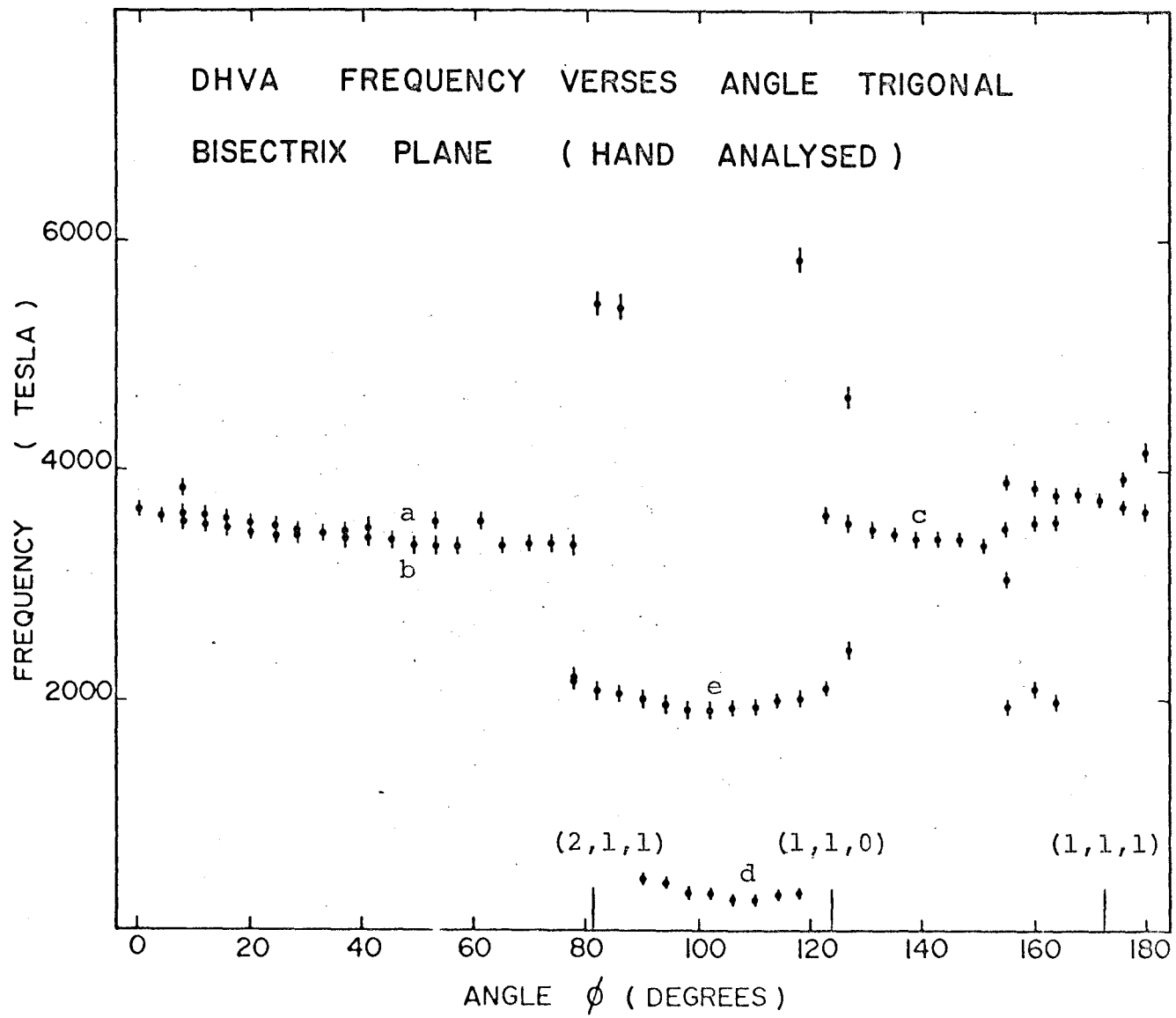
DHVA FREQUENCY VERSES ANGLE TRIGONAL
BISECTRIX PLANE (HAND ANALYSED)
FREQUENCY (TESLA)
6000
4000
2000
a
b
c
d
e
(2,1,1)
(1,1,0)
(1,1,1)
0
20
40
60
80
100
120
140
160
180
ANGLE ϕ (DEGREES)

Figure 13

analyzed by the fourier transform method. The results of this analysis are shown in Figures 14 and 15. All of these data are tabulated in Appendix A.

The magnetic field was measured by monitoring the magnet current by means of manganin shunts. The shunts were constructed by the Bach-Simpson Corporation with total resistance variations within 0.1% and 0.01% due to time and total temperature variations. The absolute current to field calibration was performed at 2.4 tesla using the electron spin resonance signal to DPPH (Diphenyl picryl hydrazyl) and a 4 mm waveguide apparatus capable of vertical movement. The point of maximum field was determined and the field and microwave frequency were measured several times and averaged. Non-linearities between the magnet current and the magnetic field constituted the major portion of the absolute error. The less accurate shunt was used for the hand analyzed data while the voltage across the 0.01% shunt was amplified and smoothed with a one second time constant for the tape-recorded data.

The fourier transform method is a powerful tool in the analysis of dHvA results. A comparison of Figures 13 and 14 shows that many more frequencies were analyzed using the fourier analysis than using hand analysis although the signal to noise ratio of the data was approximately equal. Several traces ranging in signal to noise, magnetic field range and sweep speed were chosen to demonstrate this point.

Figure 16 shows a chart recorder trace of low frequency

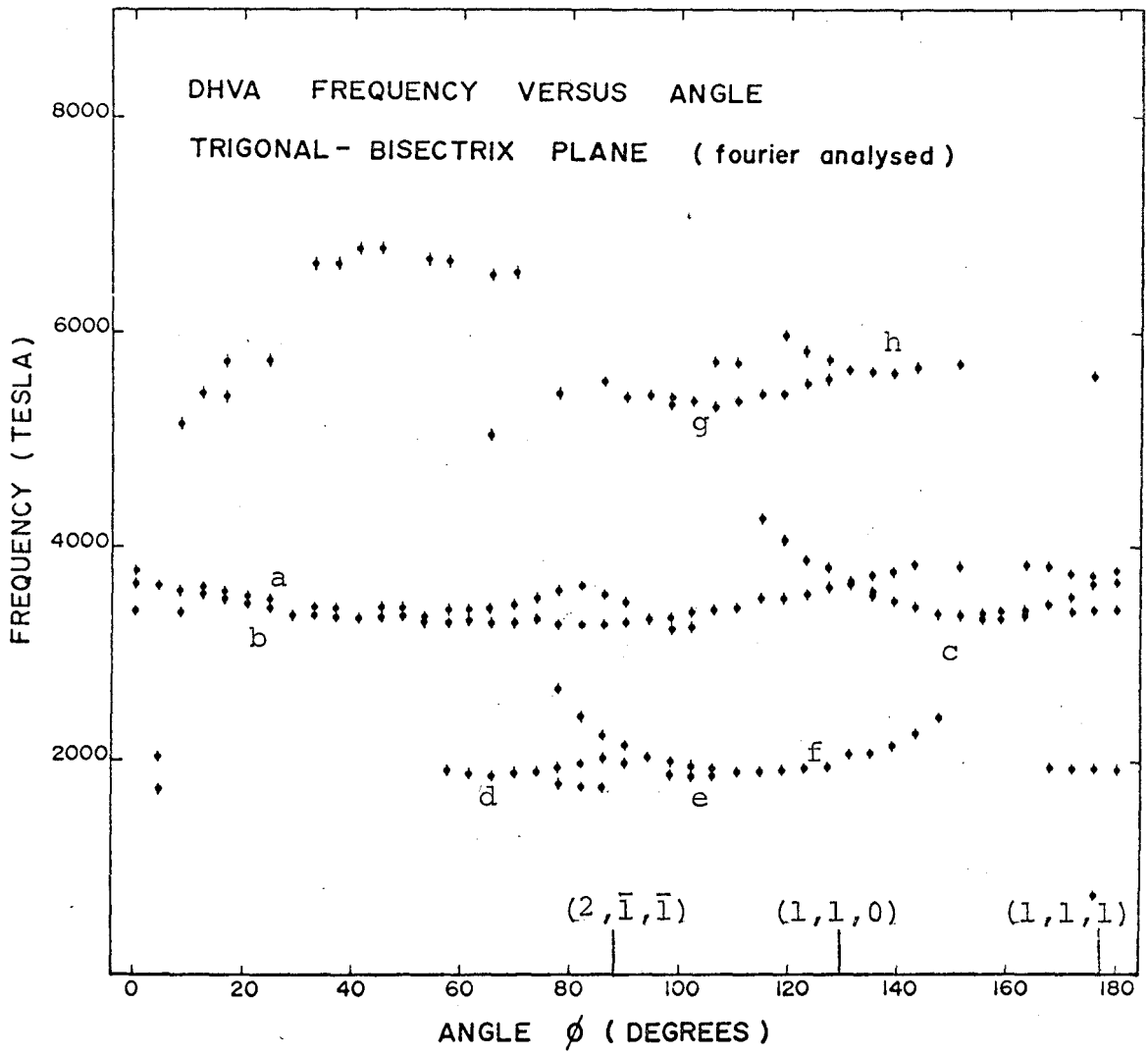
DHVA FREQUENCY VERSUS ANGLE
TRIGONAL - BISECTRIX PLANE (fourier analysed)
FREQUENCY (TESLA)
8000
6000
4000
2000
a
b
c
d
e
f
g
h
(2,1̄,1̄)
(1,1,0)
(1,1,1̄)
0
20
40
60
80
100
120
140
160
180
ANGLE ϕ (DEGREES)

Figure 14

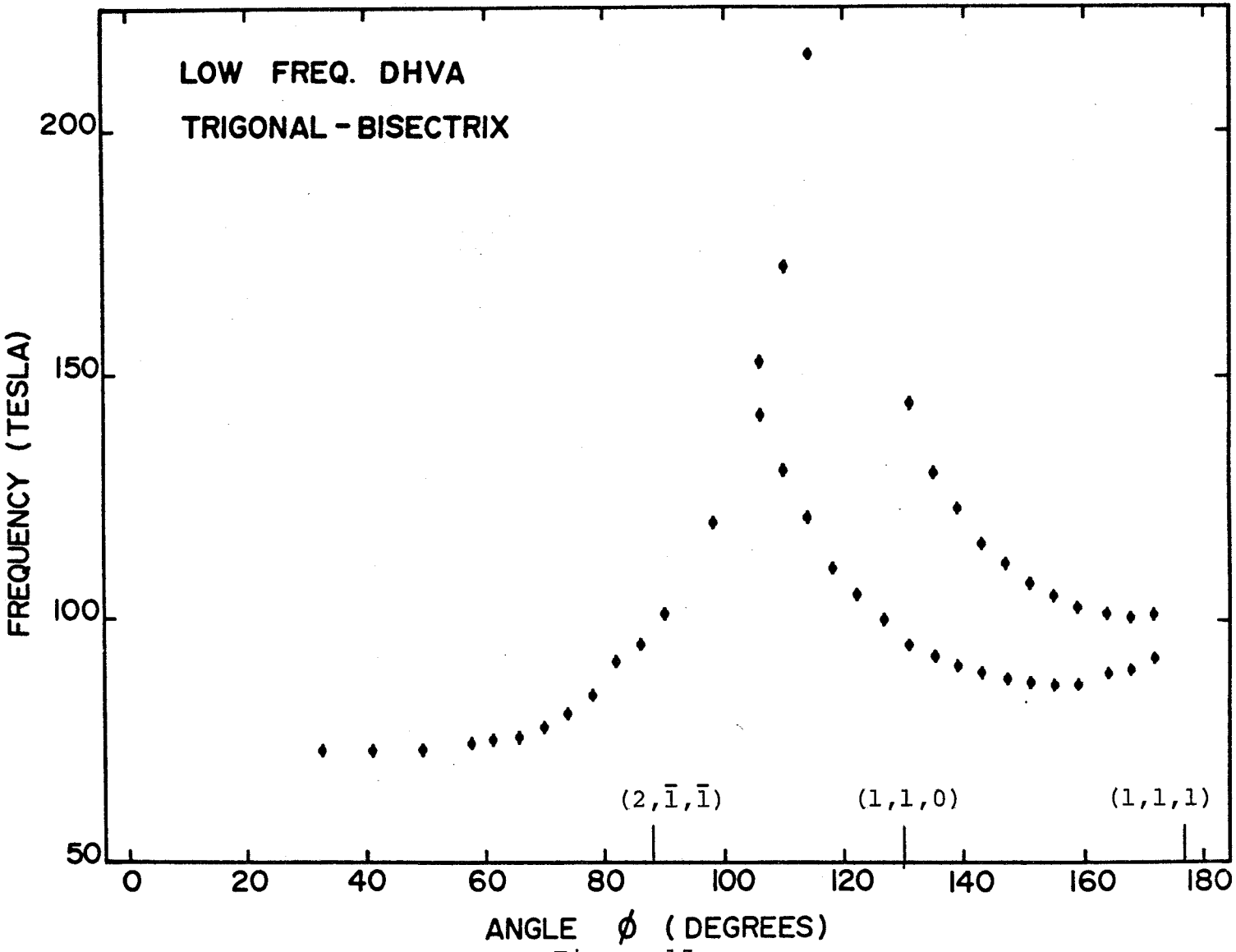
LOW FREQ. DHVA
TRIGONAL - BISECTRIX
FREQUENCY (TESLA)
200
150
100
50
0
20
40
60
80
100
120
140
160
180
(2,$\bar{1}$,$\bar{1}$)
(1,1,0)
(1,1,1)
ANGLE ϕ (DEGREES)
Figure 15

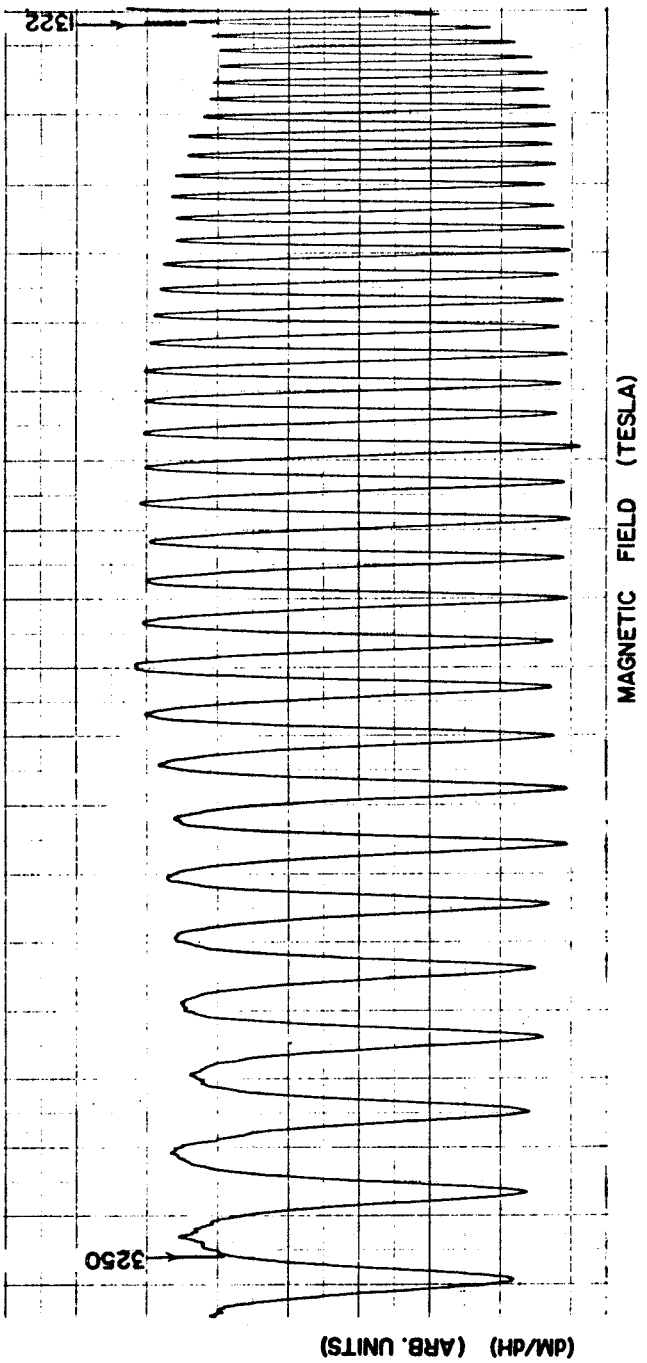

Figure 16

Sample Low Frequency Trace

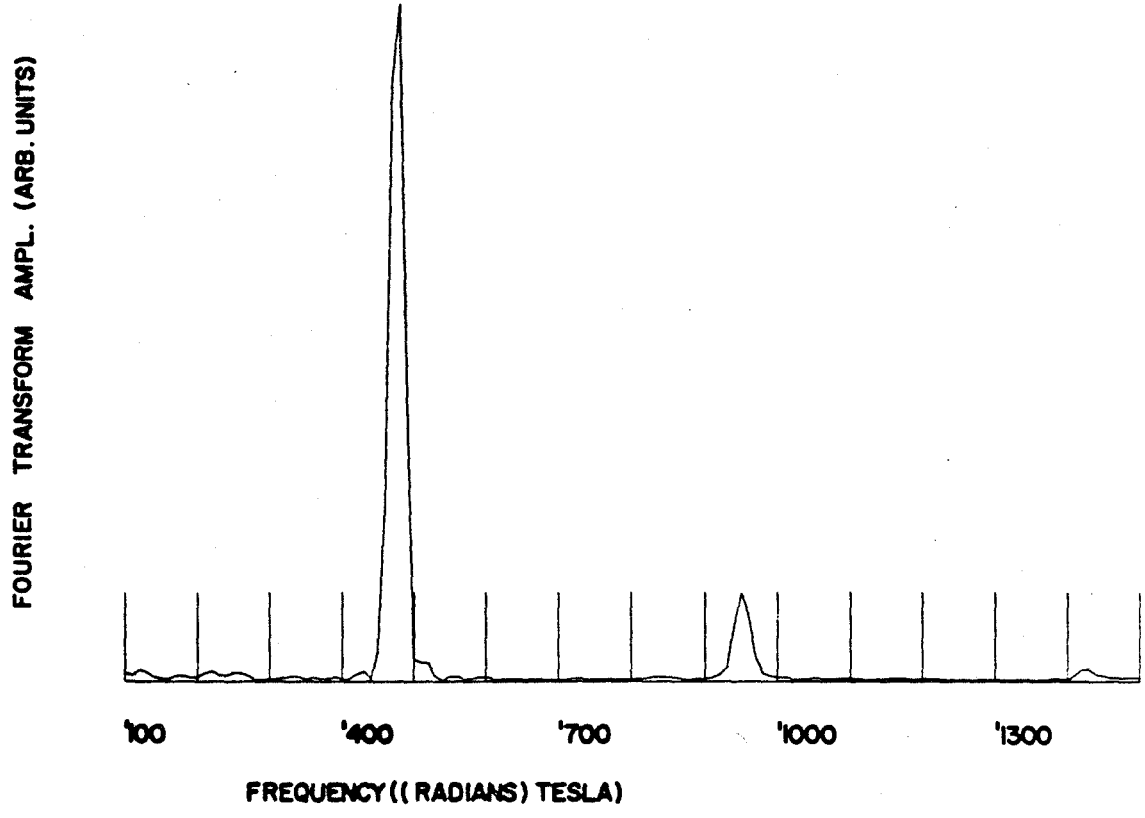

Figure 17

Sample Low Frequency Analysis

β oscillations with a rather high signal to noise ratio. The field markers on the trace are in millitesla. Detection in this case was at the fundamental of the 400 HZ modulation frequency. The noise level of the fourier power spectrum output, shown in Figure 17, and the sharpness of the peak, demonstrates the accuracy with which a low noise frequency may be determined. As the fourier program used in this analysis dictated that the frequency scale on the horizontal axis of the output be in radians tesla, it was necessary to divide the frequency of the Fourier transform plot by 2π to obtain frequencies in tesla. Figures 18 and 19 show a trace dominated by a γ oscillation and the corresponding analysis respectively. These demonstrate the ability of the transform method to discriminate between several frequencies in the same general range. The very low frequency oscillation , due to the β orbit, was below the range of the analysis. Five other oscillations were resolved. Not only would five frequencies have been impossible to analyze by hand from one trace, but the ambiguity inherent in beat analysis by hand, of whether a beat represents a higher or lower frequency than the dominant oscillation, has been removed.

Figure 20 shows a trace recorded using a detection frequency of 1600 Hz, the third harmonic of the 400 Hz modulation frequency, which shows a dominant α oscillation. The higher frequency peaks on the analysis, shown in Figure 21,

Figure 18

Sample Medium Frequency Trace

Figure 19

Sample Medium Frequency Analysis

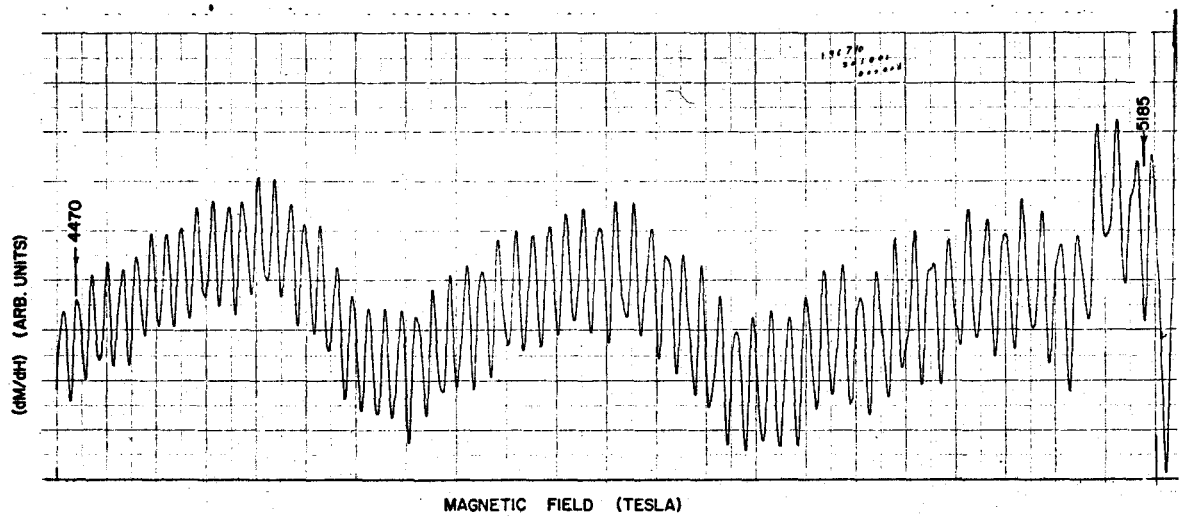
4470
5185
(dM/dH) (ARB. UNITS)
MAGNETIC FIELD (TESLA)

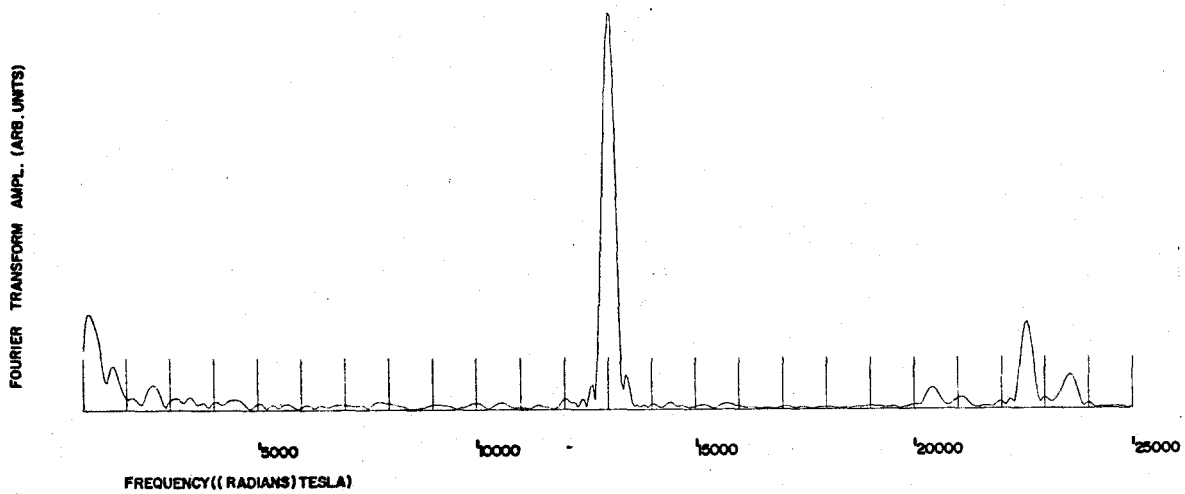
FOURIER TRANSFORM AMPL. (ARB. UNITS)
5000
10000
15000
20000
25000
FREQUENCY((RADIANS)TESLA)

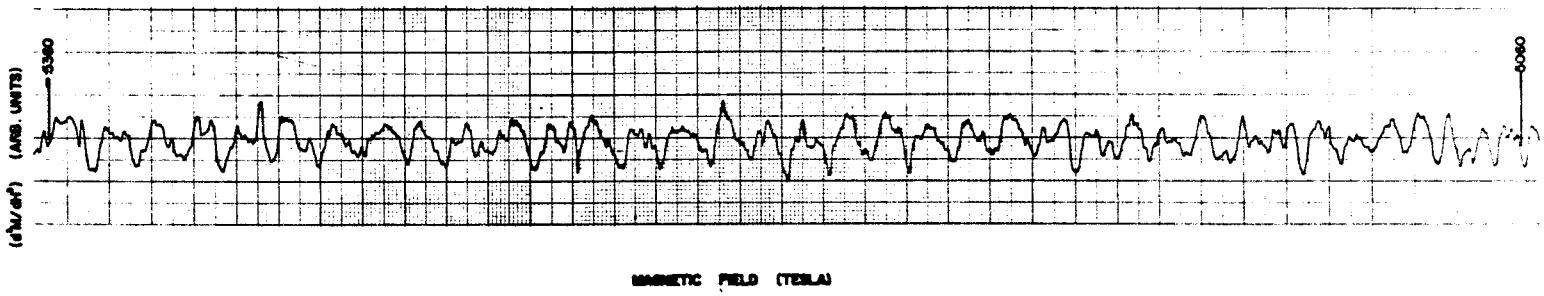

Figure 20

Sample High Frequency Trace

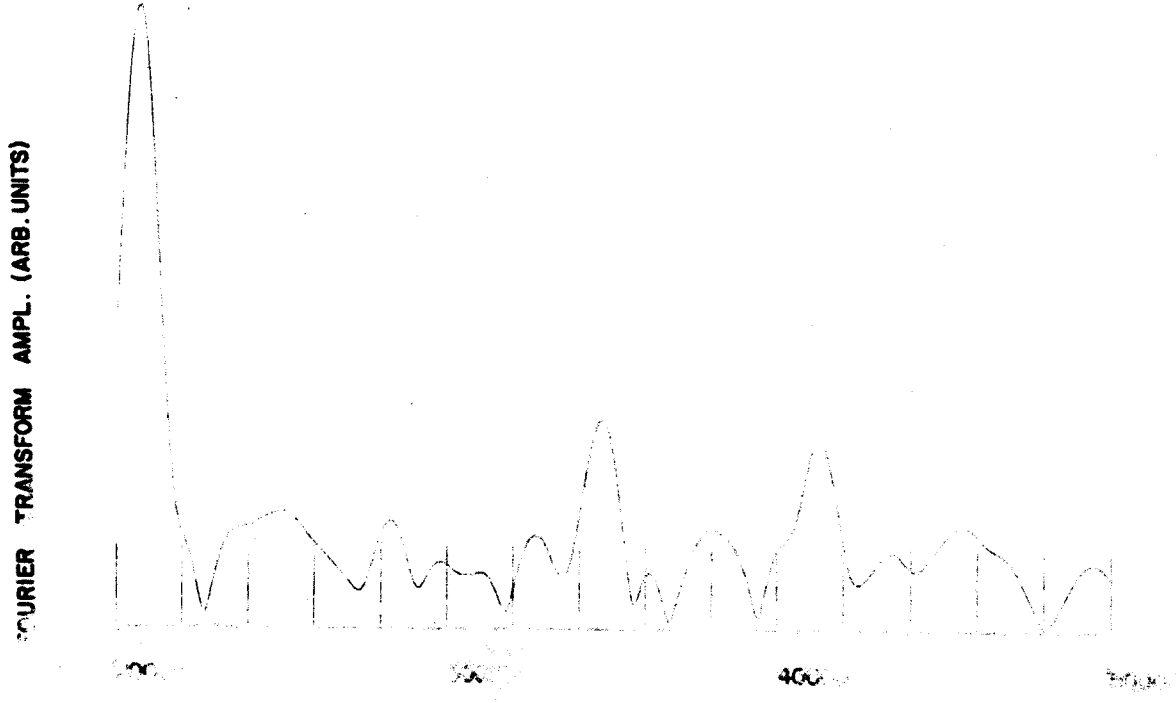

correspond to the X-face electron orbit and the μ hole orbit. The presence of these peaks on the analysis output plot indicates the ability of the fourier method to discriminate between signal and random noise. It was estimated that a signal to noise ratio of 1:10 resulted in a reliable analysis of the signal frequency in most cases. The difference between this and the minimum ratio of approximately 1:50 which might have been expected for a fifty oscillation trace was due to inaccuracies in the field calibration.

Points were retained if the amplitude of the corresponding peak in the power spectrum was greater than twice the noise level. Thus some points were included which could have been due to noise. Some of the data points represent averages of closely spaced values obtained for separate runs of the same orientation and of separate analyses of some of the data recorded on magnetic tape. In all cases the spread of the values which were averaged was within the error bars given.

The angle Ø was the angle of the sample orientation within the plane of the data. Ø=0 in this plane was arbitrary

In the trigonal-binary plane, shown in Figure 12, the data divided into groups of points above and below 3000 tesla. One line of points, labelled 'c'; could be followed across the graph, while signals could be analysed for only the lower sections of the 'a' and 'b' curves. The data labelled 'd' extended approximately from Ø = 70 degrees to

ϕ = 115 degrees. Beyond these angles the signal was lost in the other oscillations. At each end of the sequence of points labelled 'd' were two groups of points labelled 'e' and 'f' which were of low signal to noise ratio and difficult to analyze in the presence of the 'a', 'b' and 'c' data sequences.

The data shown in Figure 13 were analyzed by hand from traces taken with the sample oriented such that the field was in the trigonal-bisectrix plane. Other traces were recorded on magnetic tape for the same orientation and analyzed using the fourier transform method. The angle for which 'a' and 'b' crossed was more easily determined by hand analysis of the beats and was found to be ϕ = 33 degrees.

The data labelled 'a', 'b' and 'c' in Figure 14 were groups of closely spaced peaks on the fourier plots of traces recorded using the fundamental and first harmonic of the modulation frequency. The detection frequencies used to obtain the points above 4000 tesla, including the sections labelled 'g' and 'h', were 1200 and 1600 cps for a modulation frequency of 400 cps. Sections 'd', 'e', 'f', 'i' and 'j' were obtained using only detection of the fundamental. Even though the amplitude of the 'f' oscillations was considerably larger than the signal giving rise to the 'd' and 'e' sections it was possible to resolve the 'e' and 'f' oscillations using the fourier program. Both the 'i' and 'j' data points were of low amplitude.

Figure 15, which includes the low frequency trigonal

bisectrix data, indicates three minimum areas and no low amplitude signals.

CHAPTER VI

ANALYSIS OF THE F.M.T. MERCURY RESULTS

Different sections of the Fermi surface were approximated by hyperboloids or ellipsoids of revolutions. This immediately indicated whether $\left|\frac{\partial^2 A}{\partial k_z^2}\right|_{A=A_o}$ was negative or positive for the section of interest. Where the Fermi surface was described by

$$\frac{x^2+y^2}{a^2} \pm \frac{z^2}{b^2} = 1 \qquad \text{IV.1}$$

it was possible to determine the constants a and b. Since the transverse sections of the surface were not circular, the ratio b/a indicated the amount of flare in the plane of magnetic field rotation.

The areas of intersection of a plane By + Cz = 0 and the hyperboloid or ellipsoid of revolution were fitted to the experimental areas of cross-section by a least mean square method due to A.E. Dixon[36] and R. G. Poulsen[37].

A. THE β ORBIT

The data for the β arms agreed very well with Brandt and Rayne, and with Poulsen. The minimum frequency of 73 tesla corresponded to an area of 0.0070 $(A.U.)^{-2}$. None of the low frequency β_2 oscillations suggested by Brandt and Rayne were detected in this experiment.

These data were used to check the orientation of the trigonal-bisectrix plane . The plane was found to be rotated by approximately 6 degrees about an axis close to the (1,0,0) direction of reciprocal space. This misalignment is outside the range of the error of the Laué orientation and a similar misalignment of the binary-trigonal data was detected. One possibility is that the surface of the crystal, or a crystallite on the surface that was used for x-ray alignment was slightly misoriented relative to the volume.

B. THE τ AND γ ORBITS

The points shown in Figure 22(a), which show the 'd' section of the trigonal-binary plane, were attributed to the τ orbit. A minimum of 1570 $\pm$ 10 tesla occurred at the binary axis. The fit shown by the solid line indicated a rather wide neck, 0.94 being the b/a ratio of the fitted hyperboloid.

When the 'd' section of Figure 15 was fitted to an hyperboloid of revolution with the hyperboloidal axis 30° out of the plane of the data, the extrapolated minimum area of the hyperboloid was 1580 $\pm$ 20 tesla. The fit is shown in Figure 23(a). This was not positive identification of the 'd' section as the 'f' section resulted in an almost identical least square hyperboloid. In this plane the τ orbit was expected to give rise to two sequences of points, each of which would be doubly degenerate . Brandt and Rayne[31] have analyzed

(a)

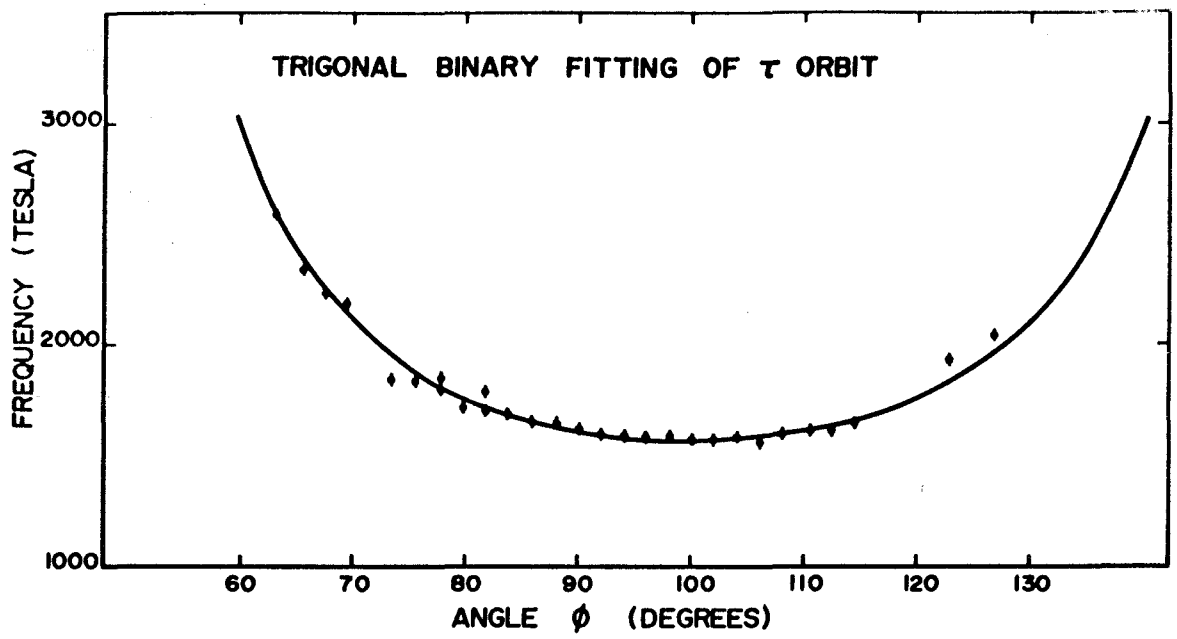

(b)

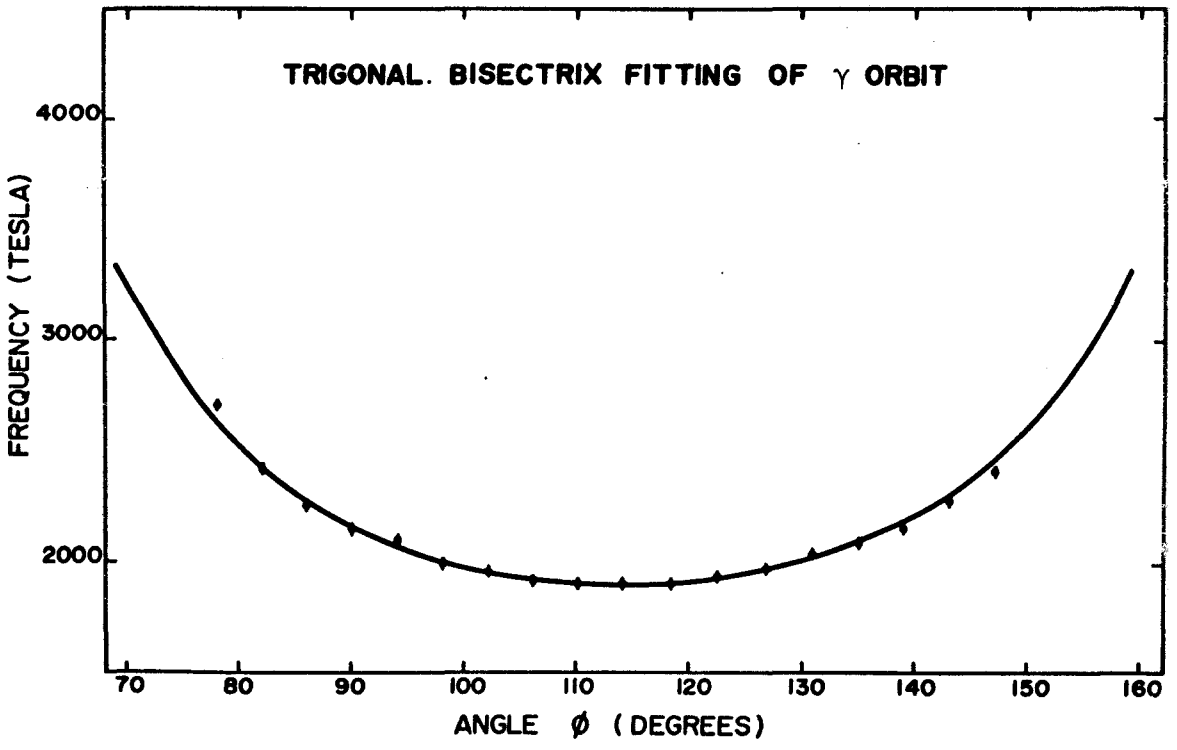

Figure 22

Least Mean Square Fit to
Hyperboloid of Revolution

(a)

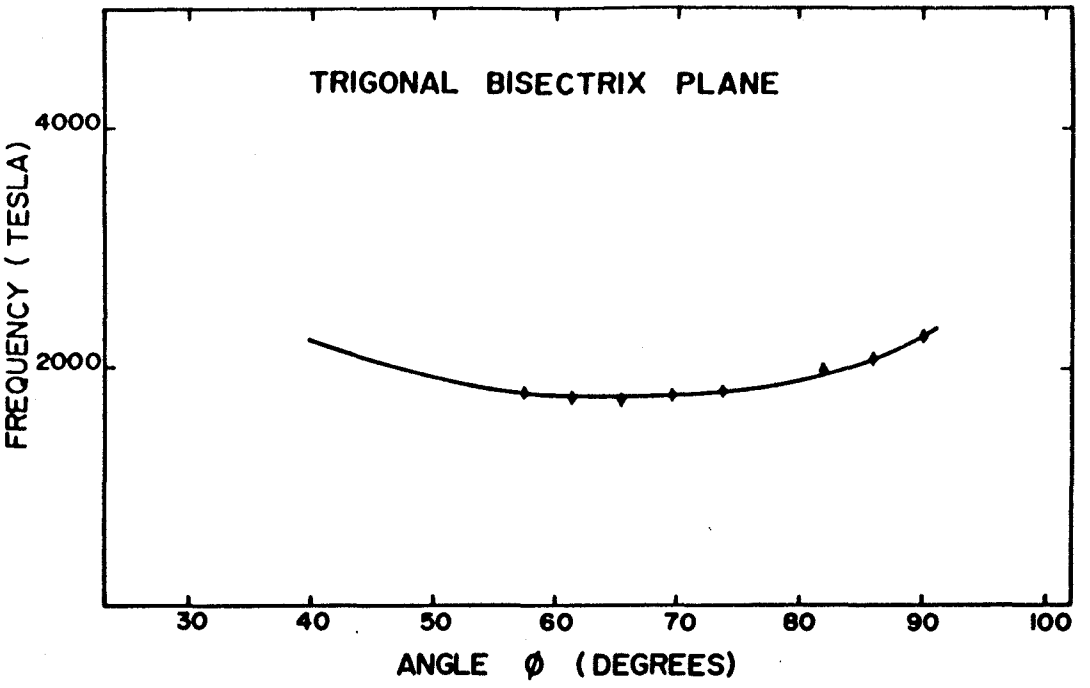

(b)

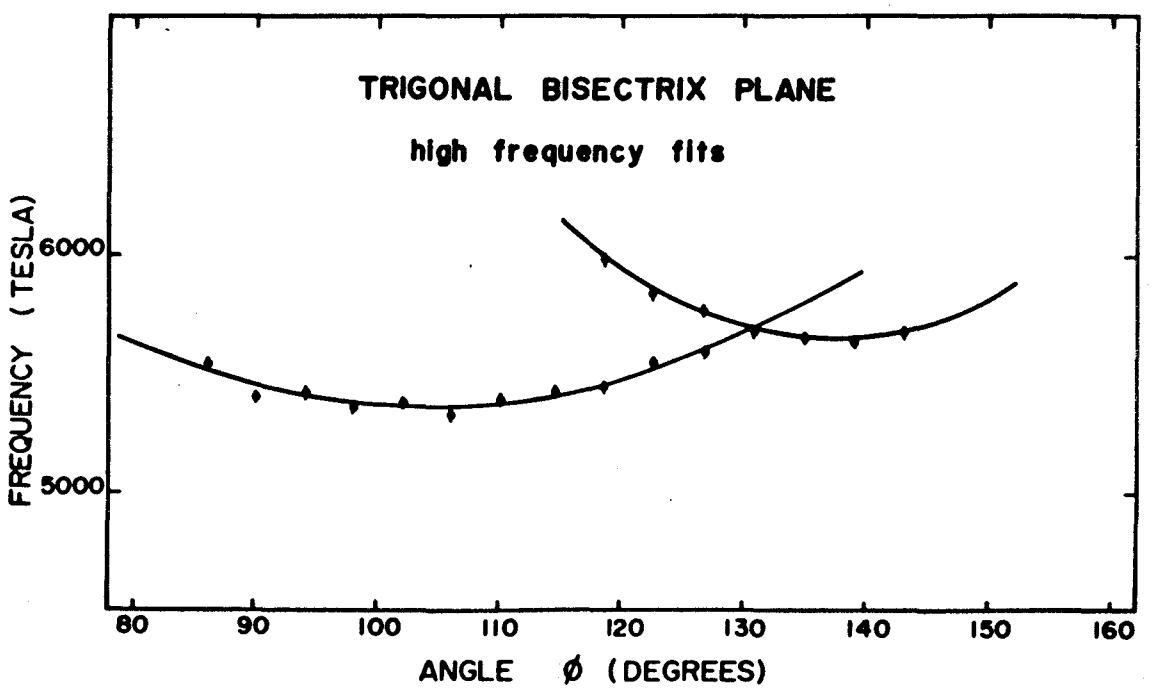

Figure 23

Least Mean Square Fit to
Hyperboloid of Revolution (Trigonal-Bisectrix)

their data for the binary-bisectrix plane. Their published data showed minimum areas at both the binary and bisectrix axes in this plane, both of which were ascribed to the τ orbit by the authors. Since the τ orbit was not able to explain a minimum area at a direction near the bisectrix axis, and since the γ orbit should have a minimum near this direction, this section of Brandt and Rayne's data centred about the bisectrix axis was assigned to the γ orbit. The data labelled 'f' on Figure 15, which were also due to the γ orbit were fitted to an hyperboloid, shown in Figure 22(b). b/a was determined to be 0.8, in qualitative agreement with this assignment. The minimum of the γ orbit was determined to be 28 degrees from the bisectrix axis toward the (1,1,0) direction. The γ orbit also gave rise to the groups of points labelled 'e' and 'f' in Figure 12. Not only did the frequency of these groups agree well with the value of 2300 tesla derived from the hyperbolic fit of the trigonal bisectrix data, but also the small variation of frequency with angle in these groups was expected due to the 28 degree angle between the bisectrix axis and the direction of the minimum area.

The section of data labelled 'd' and 'e' in Figure 15 were attributed to the τ orbit. Although the number of points 'e' were not sufficient to allow a separate least squares fit, the symmetry of the two sequences about the bisectrix axis supported this assignment. The minimum areas in

this plane occurred at plus and minus 20 $\pm$ 2 degrees either side of the bisectrix direction. Although it is possible to also assign the sequence 'f' in Figure 15 to the τ orbit, this was considered unlikely due to its large amplitude, angular extent and the large angle between the normal to the minimum area and the bisectrix direction. Thus the τ orbit minimum area of 0.15 $(A.U.)^{-2}$ was normal to the binary axis.

C. THE α ORBIT

Some difficulty was encountered in obtaining signals corresponding to the larger areas of the electron lenses. This was not due to the residual misalignment of the trigonal bisectrix plane as the plane of the data crossed the trigonal bisectrix very nearly at the maximum frequency of the α oscillations. Part of the problem stemmed from the fact that the maximum frequency of the α oscillations was almost exactly twice that of the other α oscillations at that orientation. It was possible, however, to distinguish between the harmonic of the lower frequency and the fundamental of the higher frequency because there was a detectable beat between them. The accuracy of this determination of the frequency by this method was very low and subject to the uncertainty of whether the detected fundamental was higher or lower than the harmonic. In some cases it was possible to separate these frequencies using the fourier program but with very poor accuracy. Figure 24 shows the fit obtained for an oblate ellipsoid of revolution.

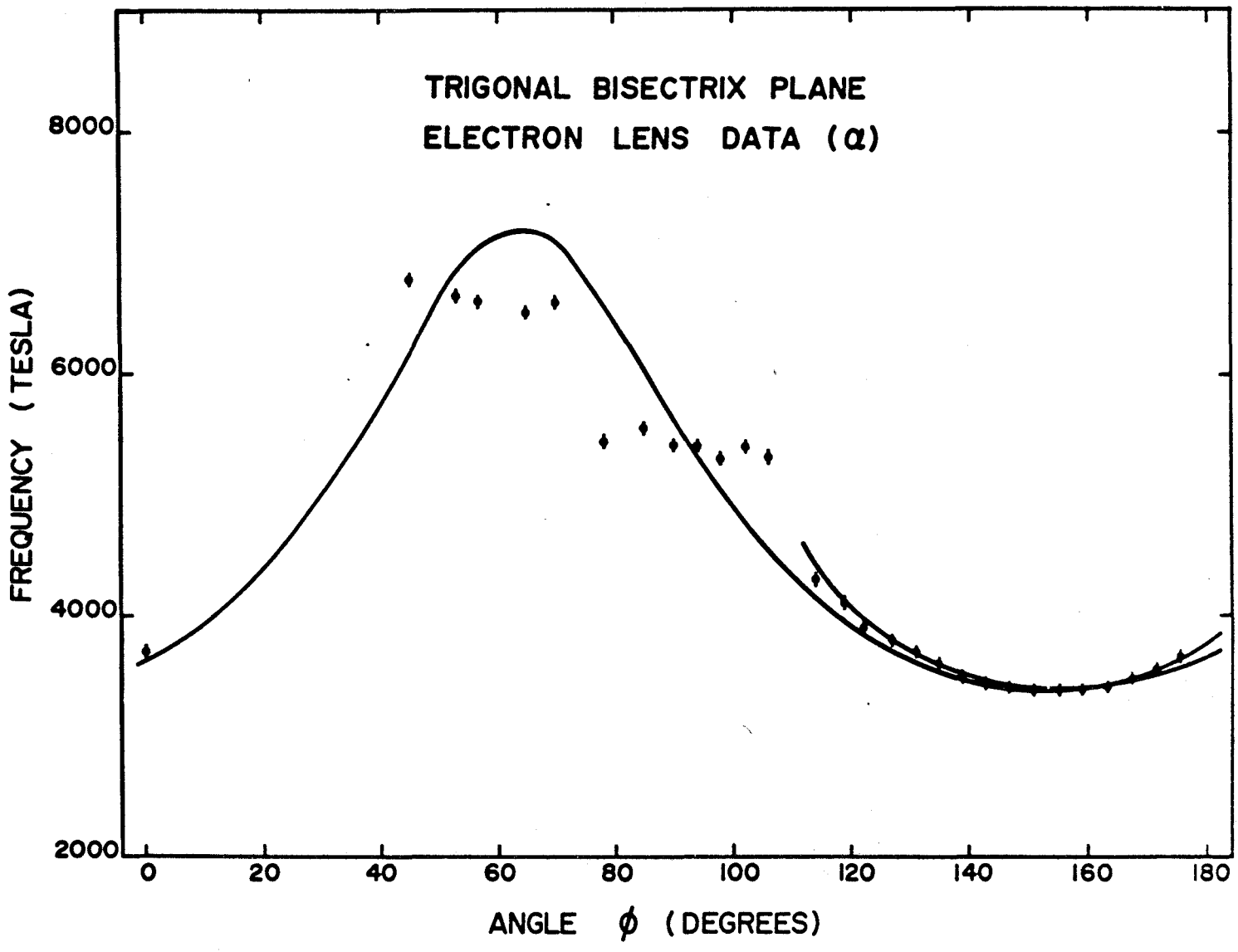

Figure 24

Least Mean Square Fit
to Ellipsoid of Revolution

Including the points at the top of the curve gave the lower curve, while the upper solid curve resulted when only the lower frequency points were included. The difference indicated that the second zone electron lenses were not truly ellipsoidal.

The maximum frequency of 7000 ± 200 tesla corresponded to an area of $(A.V.)^{-2}$ while the minimum area was 3300 ± 20 tesla, or 0.32 $(A.U.)^{-2}$. The least mean square ellipsoid semi-major axis was 0.22 A.U. while the semi-major axis was 0.46 A.U. The volume of the approximate ellipsoid was 0.20 $(A.U.)^{-3}$ whereas the volume of the corresponding free electron spherical segments was 0.38 $(A.U.)^{-3}$. The volume of the first zone hole surface was, therefore, also equal to approximately 0.20 $(A.U.)^{-3}$, roughly one half that given by the free electron model. The corresponding densities of the carriers was $4.5 \times 10^{27} \pm 1.0 \times 10^{27}$ electrons/m^3 and the same density of holes.

D. THE X-FACE NECK

Several other series of oscillations were detected by the fourier method. One of these, shown in Figure 23(b) was centered at ϕ = 137 degrees in the trigonal bisectrix plane. The minimum frequency in this plane was 5650 tesla and the ratio b/a = 0.57, indicating a short neck. This was attributed to the connecting neck in the rectangular X-face, the axis of which should have been 42 degrees from the trigonal in this plane.

The area of the minimum of this orbit in k-space was

0.54 $(A.U.)^{-2}$. Keeton and Loucks have indicated this orbit to be a rounded square. A square of the above area has sides of 0.73 $(A.U.)^{-1}$.

E. OTHER FERMI SURFACE SECTIONS

When the points labelled 'g' of Figure 15 were fitted it was found that they produced a cylinder of area 5350 tesla,or 0.51 $(A.U.)^{-2}$ with its axis 16 $\pm$ 10 degrees from the bisectrix axis toward the (1,1,0) direction. This section of the data was tentatively assigned to the μ orbit. Some doubt remained about this assignment because of the large scatter of the points, the cylindrical nature of the fit, and the displacement of the axis of the cylinder toward, rather than away from, the (1,1,0) direction. As the angle of the minimum was determined by the details of the Fermi surface for this orbit, no orientation close to the bisectrix axis could be eliminated.

Due to the small number of points involved, the groups of points about the trigonal axis of Figure 15, labelled 'i' and 'j' were not used for fitting. The frequencies of these sections were 3400 and 1920 tesla respectively, corresponding to areas of 0.33 and 0.18 $(A.U.)^{-2}$. The lower value was considered more likely to be the area of the T-face hole for the following reasons. First, the fourier analysis peaks corresponding to 'j' were not subject to the interference of the side bands of large nearby signals as were the higher frequencies. Brandt and Rayne[31] have published

results indicating a possible area of 0.24 $(A.U.)^{-2}$ at approximately 10 degrees from the trigonal. Also Datars[28] has suggested an area of 0.06 $(A.U.)^{-2}$ from magnetoresistance results.

F. SUMMARY

Table IV showing a summary of the data on the orbits, indicated that there was at least a tentative assignment of data to each of the expected orbits. The estimated errors indicated the accuracy of the areas. The assignments most in doubt were those of the μ orbit and the T-face neck orbit.

The α orbit analysis showed that the second zone electron lense volume was approximately one half of the free electron value. This is in qualitative agreement with Pippard's[24] estimate that the area of the Fermi surface was one half of the free electron sphere. No section of the Fermi surface was assigned to the data labelled 'd' on Figure 14. These points were not reproduced by the fourier analysis and no explanation was found for their presence. None of the other points formed sequences so they were assumed to be due to random noise, particularly as the amplitudes of these oscillations were close to the noise level in all cases.

In the analysis of the results of this experiment a geometric approach has been used. Brandt and Rayne, on the other hand, fitted their data by a pseudo-potential method. In order to obtain a significant improvement to their fit it

TABLE IV

Summary of Orbit Data

Orbit	Min. Freq. (tesla)	Min. Area $(A.U.)^{-2}$	Dir. of Normal to Min. Area in reciprocal sphere	b/a	Nature of Orbit
β	73 ± 0.5	0.0070	In intersection of X-face plane and trigonal bisectrix plane		Almost cylindrical hole surface arm
τ	1570 ± 10	0.150 ± 0.001	binary	0.9	hole
γ	1900 ± 10	0.182 ± 0.001	28° from bisectrix toward (1,1,0)	0.77	hole
α	3300 ± 20	0.32	In plane normal to (1,0,0) axis	0.47	electron lense
Neck at X	5650 ± 50	0.54 ± 0.005	(1,1,0)	0.57	electron neck
μ	5350 ± 100	0.51 ± 0.001	approx. bisectrix		hole
Neck at T	1920 ± 100	0.18 ± 0.01	(1,1,1)		electron neck

would have been necessary to use a pseudo-potential calculation which accounted for the large spin-orbit effects expected because of the d-states of mercury. Also a calculation of this type would require several accurately determined parameters of the electron lenses, as well as the parameters of the other orbits which have been given in this thesis, in order to both evaluate and check the pseudo potential parameters. The geometric analysis provided some of the data that would be necessary for a detailed pseudo-potential fit while allowing a detailed qualitative comparison with the model derived from the augmented plane wave calculation of Keeton and Loucks. It was possible to extend Brandt and Rayne's assignment of orbits to include all the expected orbits, at the same time eliminating one contradiction of their assignment.

CHAPTER VII

CONCLUSIONS

A method of determining the orientation and extent of the open orbits in compensated and uncompensated metals was developed. The method did not involve electrical leads to the sample as the currents were induced by rotation of the magnetic field. Because of this, the sample shape was not critical provided it was regular. Consequently the method is useful for orientation of samples of metals supporting open orbits, particularly if the sample geometry is determined by another experiment. A qualitative theory was developed to explain the major features of the experiment.

An attempt was made to detect temperature effects on the effective mass and the Dingle temperature for the β oscillations of mercury. Careful amplitude measurements were made from $1.25^{\circ}K$ to $4.2^{\circ}K$ and no effect was found in this temperature range.

Orbits of the Fermi surface of mercury have been observed and their parameters evaluated using a field modulation dHvA apparatus. The β orbit was observed in agreement with Brandt and Rayne[31] but no β_2 oscillations were observed. Signals due to both the τ and γ orbits were observed. In spite of their proximity in direction and frequency, the

minimum areas of the τ and γ orbits were found to be 0.150 ± 0.001 $(A.U.)^{-2}$ and 0.182 ± 0.001 $(A.U.)^{-2}$ respectively. The minimum of the τ orbit was at the binary axis while the γ orbit minimum was 28 degrees toward the (1,1,0) direction from the bisectrix axis. The neck orbit about the X point of the Brillouin zone was observed at the (1,1,0) direction, as expected, with a minimum area of 0.54 ± 0.005 $(A.U.)^{-2}$. Tentative identification was made of data for the μ orbit with a minimum area of 0.51 ± 0.01 $(A.U.)^{-2}$ approximately normal to the bisectrix axis, and for the T-face neck orbit with a minimum area of 0.18 ± 0.01 $(A.U.)^{-2}$ normal to the (1,1,1) axis.

The data from the electron lenses were used to estimate the volume of the second zone lenses to be approximately one half the free electron volume. Since mercury is a compensated metal, the volume enclosed by the first zone hole surface was also about one half the free electron value. The density of each of the carrier types was $4.5 \times 10^{-27} \pm 1.0 \times 10^{27}$ carriers/meter^3.

APPENDIX A

TABLE OF MERCURY dHvA DATA

TRIGONAL-BINARY PLANE

(HAND ANALYSIS)

Turns	Angle (Deg) ($\pm$0.1 deg)	τ and γ (tesla)	α (tesla)
0	0		3536 4005
1/4	2.0		3578 3980
1/2	4.1		3592 3904 3904
3/4	6.1		3612 3886 3876
1	8.2		3675 3884 3807
1-1/4	10.2		3690 3873 3782
1-1/2	12.3		3720 3868 3761
1-3/4	14.3		3780 3938
2	16.3		3680 3818 3862
2-1/4	18.3		3655 3865 3865
2-1/2	20.4		3606 3846 3930

TABLE OF MERCURY dHvA DATA (continued)

Turns	Angle (Deg) (± 0.1 deg)	τ and γ (tesla)	α (tesla)
2-3/4	22.4		3568
3	24.5		3545 3793
3-1/4	26.5		3510 3806
3-1/2	28.6		3495 3840
3-3/4	30.6		3470 3775
4	32.7		3455 3763
4-1/4	34.6		3440 3748
4-1/2	36.8		3440 3750
4-3/4	38.8		3425
5	40.8		3420
5-1/4	42.9		3420
5-1/2	44.9		3415
5-3/4	46.9		3475 3667
6	49.0		3445 3599
6-1/4	51.0	2587	3450 3551
6-1/2	53.1	2577	3510 3595

TABLE OF MERCURY dHvA DATA (continued)

Turns	Angle (Deg) (±0.1 deg)	τ and γ (tesla)	α (tesla)
7	57.2	2486	3520 3480
7-1/4	59.2	2405	3525
7-1/2	61.3	2350 2404	3550 3525 3475
7-3/4	63.3	2600	3630 3484
8	65.4	2300 2346	3630 3593 3454
8-1/4	67.4	2240	3650
8-1/2	69.5	2200 2243	3690 3605 3373
8-3/4	71.5		3405 3797
9	73.6	1847 2259	3330 3787 3715 3367
9-1/4	75.6	1832	3330 3811
9-1/2	77.7	1798 1855	3320 3340 3787
9-3/4	79.7	1715	3290
10	81.8	1704 1785	3280 3330 3889
10-1/4	83.8	1694	3278

TABLE OF MERCURY dHvA DATA (continued)

Turns	Angle (Deg) (±0.1 deg)	τ and γ (tesla)	α (tesla)
10-1/2	85.9	1663 1708	3265 3280
10-3/4	88.0	1657	3255
11	90.0	1629 1673	3258 3270
11-1/4	92.0	1594	3241
11-1/2	94.1	1600 1630	3240 3260
11-3/4	96.1	1579	3220
12	98.2	1588 1604	3240 3240
12-1/4	100.2	1582	3238
12-1/2	102.3	1585 1569	3240 3238
12-3/4	104.2	1581	3240
13	106.3	1513 1553	3305 3210
13-1/4	108.3	1572	3285
13-1/2	110.4	1620 1598	3240 3265
13-3/4	112.4	1620	3265
14	114.5	1643 1637	3285 3275
14-1/4	116.5		3320
14-1/2	118.6		3300
14-3/4	120.6		3321
15	122.7	1950	3335

TABLE OF MERCURY dHvA DATA (continued)

Turns	Angle (deg.) ($\pm$0.1 deg)	τ and γ (tesla)	α (tesla)
15-1/4	124.7		3380
15-1/2	126.8	2055	3355 4642
16	130.8		3365
16-1/2	134.9	2045	3395 3903
17	139.0	2058 2070	3440 3902
17-1/2	143.1	2132	3595 3505 3874 (3560)
18	147.2	2225	3560 3605 3161
18-1/2	151.3		3475 3639
19	155.4		3440 3712
19-1/2	159.5		3445 3420 3786
20	163.6		3415 3813
20-1/2	167.7		3420 3864
21	171.8		3424 3840
21-1/2	175.9		3460
22	180.0		3505 4128

TRIGONAL-BISECTRIX PLANE

(HAND ANALYSIS)

Turns	Angle (Deg.) (± 0.1 deg)	Low Frequencies (tesla)	τ and γ (tesla)	α (tesla)
0	0			3650 3650
1/4	2.0			3610 3670
1/2	4.09			3595 3600 3658
3/4	6.1			3545 3625
1	8.18			3565 3614 3842
1-1/2	12.26			3535 3590
2	16.33			3480 3540
2-1/2	20.4			3455 3504
3	24.5			3440 3470
3-1/2	28.6			3440 3456
4	32.7			3440 3451
4-1/2	36.8			3420 3455
5	40.8			3400 3469
5-1/2	44.9			3380 3490
6	49.0			3340 3360 3505 3520

TRIGONAL-BISECTRIX PLANE (continued)

Turns	Angle (Deg.) (±0.1 deg)	Low Frequencies (tesla)	τ and γ (tesla)	α (tesla)
6-1/4	51.0			3340
6-1/2	53.1			3350 3540
6-3/4	55.1			3360
7	57.2			3350
7-1/4	59.2		1790	3320
7-1/2	61.3			3555
7-3/4	63.3		1790	3330
8	65.4		1755	3325 3350
8-1/2	69.5			3350
8-3/4	71.5			3340
9	73.6			3360
9-1/2	77.7		2135 2170	3340
10	81.8		2085	5460
10-1/2	85.9		2035	5430
11	90.0	449	1975	
11-1/2	94.1	399.5	1945	
12	98.2	319	1930	
12-1/2	102.3	296	1925	
13	106.3	276	1940	
13-1/2	110.4	251	1945	
14	114.5	280	1995	
14-1/2	118.6	324	2030	5840

TRIGONAL-BISECTRIX PLANE (continued)

Turns	Angle (Deg.) (±0.1 deg)	Low Frequencies (tesla)	τ and γ (tesla)	α (tesla)
15	122.7		2100	3340
15-1/2	126.8		2438	3540 4642
16	130.8			3485
16-1/2	134.9			3450
17	139.0			3425
17-1/2	143.1			3415
18	147.2			3418
18-1/2	151.3			3445
19	155.4		1950	3490 3931 3049
19-1/2	159.5		2100	3550 3847
20	163.6		1970	3780 3564
20-1/2	167.7			3790
21	171.8			3745
21-1/2	175.9			3680 3942
22	180.0			3650 4140

TRIGONAL-BISECTRIX PLANE

(MACHINE ANALYSIS)

Turns	Angle (Deg.) ($\pm$0.1 deg.)	β (tesla)	τ and γ (tesla)	α (tesla)	High Frequencies (tesla)
0	0.0		1920	3420 3675 3770	
1/2	4.09		1740 2058	3650	
1	8.18			3400 3600	5170
1-1/2	12.26			3570 3620	5440
2	16.33			3510 3590	5410 5730
2-1/2	20.4			3500 3525	
3	24.5			3440 3520	5730
3-1/2	28.6			3370	
4	32.7	72.8		3360 3390 3440	
4-1/2	36.8			3350 3410	6650
5	40.8	72.8		3330	6790
5-1/2	44.9			3340 3440	6790
6	49.0	73.7		3380 3440	
6-1/2	53.1			3370	6650
7	57.2	74.8	1905 1880	3355 3430	6620
7-1/2	61.3	75.2	1880	3320 3440	

TRIGONAL BISECTRIX PLANE (continued)

Turns	Angle (Deg.) (±0.1 deg)	β (tesla)	τ and γ (tesla)	α (tesla)	High Frequencies (tesla)
8	65.4	76.1	1876	3300 3440	5050 6550
8-1/2	69.5	77.8	1885	3290 3480	6575
9	73.6	81.2	1905	3290 3530	
9-1/2	77.7	84.0	1795 2695	3280 3600	5440
10	81.8	91.9	1760 1996 2420	3285 3650	
10-1/2	85.9	95.0	1748 2032 2263	3290 3570	5540
11	90.0	101.5	1955 2140	3300 3500	5400
11-1/2	94.1		2090	3315	5425
12	98.2	120.3	1888 2000	3240 3345	5355
12-1/2	102.2		1855 1948	3250 3380	5380 6000
13	106.2	142.2 153.1	1868 1920	3410	5325 5730
13-1/2	110.3	131.3 172.3	1908	3450	5390 5720
14	114.4	121.5 216.0	1904	3520 4280	5430
14-1/2	118.5	111.0	1908	3530 4080	5440 5980
15	122.6	106.1	1940	3575 3890	5840 5530
15-1/2	126.7	99.6	1957	3630 3810	5580 5770

TRIGONAL BISECTRIX PLANE (continued)

Turns	Angle (Deg.) (±0.1 deg)	β (tesla)	τ and γ (tesla)	α (tesla)	High Frequencies (tesla)
16	130.8	95.1 144.2	2070	3660 3670	5680
16-1/2	134.9	92.6 130.6	2088	3570 3580 3738	5640
17	138.9	91.0 123.3	2150	3500 3775	5630
17-1/2	143.0	88.7 116.4	2275	3440 3850	5690
18	147.1	88.1 111.6	2420	3390	
18-1/2	151.2	87.2 107.6		3380 3830	
19	155.3	86.8 104.5		3355 3380	
19-1/2	159.3	87.2 102.4		3378	
20	163.4	88.7 101.6		3405 3840	
20-1/2	167.5	89.4 100.9	1940	3480 3810	
21	171.6	92.1 101.6	1920	3550 3760 3400	
21-1/2	175.7		1920	3420 3660 3730	5600

BIBLIOGRAPHY

1. Bethe, H., Nature (London), 127, 336 (1931).

2. Peierls, R., Ann. Phys. Lpz., 10, 97 (1931).

3 Kohler, M., Ann. Phys. Lpz., 5, 99 (1949).

4. Chambers, R. G., Proc. Roy. Soc. A, 238, 344 (1956).

5. Lifshitz, I. M., Azbel, M., Ya and Kagonov, M. I. Soviet Physics--J.E.T.P., 3, 143 (1956).

6. Ibid, Soviet Physics--J.E.T.P., 4, 41 (1957).

7. Lifshitz, I. M. and Peschanskii, V.G., Soviet Physics--J.E.T.P., 8, 875 (1958).

8. Ibid, Soviet Physics--J.E.T.P., 11, 137 (1960).

9. Fawcett, E., Advances in Physics, 13, No. 50, 139 (1964).

10. de Haas and van Alphen, Leiden Comm. No. 212A, (1930).

11. Peierls, R., Zeit. F. Phys., 64, 629 (1930).

12. Blackman, M., Proc. Roy. Soc. (London), A166, 1 (1938).

13. Landau, L.D., Appendix to D. Schoenberg, Proc. Roy. Soc. (London), A170, 341 (1939).

14. Schoenberg, D., Phil. Trans. Roy. Soc. (London), A245, 1 (1952).

15. Schoenberg, D., Prog. in Low Temp. Phys. Vol. II, C.J. Gorter, ed. (North Holland Publishing Co. Amsterdam, 1957). 226.

16. Onsager, L., Phil. Mag., 43, 1006 (1952).

17. Lifshitz, I.M. and Kosevich, A.M., Soviet Physics--J.E.T.P., 2, 636 (1956).

18. Dingle, R.B., Proc. Roy. Soc., A211, 517 (1952).

19. Schoenberg, D., Physica, 19, 791 (1953).

20. Schoenberg, D. and Stiles, P.J. Phys. Letters, 4, 274 (1953); Proc. Roy. Soc., A281, 62 (1964).

21. Windmiller, L.R. and Priestley, M.G., Bull. Am. Phys. Soc. 119, 632 (1964).

22. Goldstein, A., Williamson, S.J. and Foner, S., Rev. Sci. Inst., 36, 1356 (1965).

23. Plummer, R.D. and Gordon, W.L., Phys. Rev. Letters, 13, 432 (1964).

24. Pippard, A.B., Proc. Roy. Soc., A191, 385 (1947).

25. Verkin, B.I., Lazarev, B.G. and Rudenko, N.S., Doklady Akad. Nauk. S.S.S.R., 80, 45 (1951).

26. Gustafson, D.R., Mackintosh, A.R. and Zaffarano, D.J., Phys. Rev.,130, 1455 (1963).

27. Ziman, J.M., Electrons and Phonons (Oxford University Press, London, 1960), 374.

28. Dixon, A.E. and Datars, W. R., Solid State Comm. 3, 377 (1965); Phys. Rev. 154, 576 (1967)

29. Dishman, J.M. and Rayne, J.A., Phys. Rev. Letter 20, 348 (1966).

30. Dixon, A.E., and Datars, W.R., Bull. Am. Phys. Soc. 11, 252 (1966).

31. Brandt, G.B., and Rayne, J.A., Phys. Rev. Letters 15, 18 (1965); Brandt, G.B., and Rayne, J.A., Phys. Rev. 148 644 (1966).

32. Keeton, S.C., and Loucks, T.L., Phys. Rev. 146, 429 (1966).

33. Bridgeman, P.W., Phys. Rev., 48, 893 (1935).

34. Barrett, C.S., Acta Cryst., 10, 58 (1957).

35. Jones, H., The Theory of Brillouin Zones and Electronic States in Crystals (North Holland Publishing Co., Amsterdam, 1960), 58.

36. Dixon, A.E., Thesis, McMaster University (1966).

37. Poulsen, R.G., Dixon, A.E.,and Datars, W.R., Bull. Am. Phys. Soc. 12, 703 (1967).

38. Pines, D., Elementary Excitations in Solids (W. A. Benjamin, Inc., 1963), 155.

39. Williamson, S.J., Foner, S., and Smith, R.A., Phys. Rev. 136, 1065 (1964).

40. Vanderkooy, J., Ph.D. Thesis, McMaster Univ. (1967).

41. Smythe, W.R., Static and Dynamic Electricity (McGraw-Hill, 1950), 390.

42. Condon, J.H., and Marcus, J.A., Phys. Rev., 134, A 446 (1964).

43. Dixon, A.E., Moss, J.S., and Datars, W.R., Mat. Res. Bull., 2, 595 (1967).

44. Berlincourt, T.G., Phys. Rev., 99, 1716 (1955).

45. Luttinger, J.M., Phys. Rev., 119, 1153 (1960); Luttinger, J.M., Phys. Rev. 121, 1251 (1961).

46. Goldstein, A., Williamson, S.J. and Foner, S., Rev. Sci. Instrum. 36, 1356 (1965).

47. Moss, S. A., Documentation supplied with programs.

48. Jones, J.C., M.Sc. Thesis, McMaster Univ. (1968).